UC Berkeley
UC Berkeley Previously Published Works

Title

Lick Observatory Supernova Search follow-up program: photometry data release of 93 Type Ia supernovae

Permalink

https://escholarship.org/uc/item/7h46n1q2

Journal

Monthly Notices of the Royal Astronomical Society, 490(3)

ISSN

0035-8711

Authors

Stahl, Benjamin E
Zheng, WeiKang
de Jaeger, Thomas
et al.

Publication Date

2019-12-11

DOI

10.1093/mnras/stz2742

Peer reviewed

Lick Observatory Supernova Search follow-up program: photometry data release of 93 Type Ia supernovae

Benjamin E. Stahl [1,2]*† WeiKang Zheng,[1]* Thomas de Jaeger [1]*‡
Alexei V. Filippenko,[1,3]§ Andrew Bigley,[1] Kyle Blanchard,[1] Peter K. Blanchard,[4]
Thomas G. Brink,[1] Samantha K. Cargill,[1] Chadwick Casper,[1] Sanyum Channa,[1]
Byung Yun Choi,[1] Nick Choksi [1] Jason Chu,[5] Kelsey I. Clubb,[1] Daniel P. Cohen,[6]
Michael Ellison,[1] Edward Falcon,[1] Pegah Fazeli,[1] Kiera Fuller,[1,6]
Mohan Ganeshalingam,[7] Elinor L. Gates,[8] Carolina Gould,[1] Goni Halevi [1,9]
Kevin T. Hayakawa,[8] Julia Hestenes,[1] Benjamin T. Jeffers,[1] Niels Joubert,[10]
Michael T. Kandrashoff,[1] Minkyu Kim,[1] Haejung Kim,[1] Michelle E. Kislak,[1,11]
Io Kleiser,[12] Jason J. Kong,[1] Maxime de Kouchkovsky,[1] Daniel Krishnan,[1]
Sahana Kumar,[1,13] Joel Leja [4] Erin J. Leonard,[1,14] Gary Z. Li,[15] Weidong Li,[1]¶
Philip Lu,[2,6] Michelle N. Mason,[16] Jeffrey Molloy,[1] Kenia Pina,[1] Jacob Rex,[1]
Timothy W. Ross,[1] Samantha Stegman,[1] Kevin Tang,[1] Patrick Thrasher,[1]
Xianggao Wang,[17] Andrew Wilkins,[1] Heechan Yuk,[18] Sameen Yunus[1]
and Keto Zhang [1]

Affiliations are listed at the end of the paper

ABSTRACT

We present *BVRI* and unfiltered light curves of 93 Type Ia supernovae (SNe Ia) from the Lick Observatory Supernova Search (LOSS) follow-up program conducted between 2005 and 2018. Our sample consists of 78 spectroscopically normal SNe Ia, with the remainder divided between distinct subclasses (3 SN 1991bg-like, 3 SN 1991T-like, 4 SNe Iax, 2 peculiar, and 3 super-Chandrasekhar events), and has a median redshift of 0.0192. The SNe in our sample have a median coverage of 16 photometric epochs at a cadence of 5.4 d, and the median first observed epoch is ∼4.6 d before maximum *B*-band light. We describe how the SNe in our sample are discovered, observed, and processed, and we compare the results from our newly developed automated photometry pipeline to those from the previous processing pipeline used by LOSS. After investigating potential biases, we derive a final systematic uncertainty of 0.03 mag in *BVRI* for our data set. We perform an analysis of our light curves with particular focus on using template fitting to measure the parameters that are useful in standardizing SNe Ia as distance indicators. All of the data are available to the community, and we encourage future studies to incorporate our light curves in their analyses.

Key words: supernovae: general – galaxies: distances and redshifts.

* E-mail: benjamin_stahl@berkeley.edu (BES); weikang@berkeley.edu (WKZ); tdejaeger@berkeley.edu (TdJ)
† Marc J. Staley Graduate Fellow.
‡ Bengier Postdoctoral Fellow.
§ Miller Senior Fellow.
¶ Deceased 2011 December 12.

1 INTRODUCTION

Type Ia supernovae (SNe Ia) are objects of tremendous intrigue and consequence in astronomy. As individual events, SNe Ia – especially those at the extremes of what has been previously observed (e.g. Filippenko et al. 1992a,b; Foley et al. 2013) – present interesting

case studies of high-energy, transient phenomena. Collectively, SNe Ia are prized as 'cosmic lighthouses' with luminosities of several billion Suns, only a factor of 2–3 lower than an L^* host galaxy of $\sim 10^{10}$ L$_\odot$. The temporal evolution of the luminosity of an SN Ia, which is powered largely by the radioactive decay chain ^{56}Ni $\rightarrow$ ^{56}Co $\rightarrow$ ^{56}Fe, is codified by light curves (typically in several broad-band filters). With some variation between filters, an SN Ia light curve peaks at a value determined primarily by the mass of ^{56}Ni produced and then declines at a rate influenced by its spectroscopic/colour evolution (Kasen & Woosley 2007). With the advent of empirical relationships between observables (specifically, the rate of decline) and peak luminosity (e.g. Phillips 1993; Riess, Press & Kirshner 1996; Jha, Riess & Kirshner 2007; Zheng, Kelly & Filippenko 2018), SNe Ia have become immensely valuable as cosmological distance indicators. Indeed, observations of nearby and distant SNe Ia led to the discovery of the accelerating expansion of the Universe and dark energy (Riess et al. 1998; Perlmutter et al. 1999), and they continue to provide precise measurements of the Hubble constant (Riess et al. 2016, 2019).

The aforementioned light-curve 'width–luminosity' relations form the basis for the use of SNe Ia as cosmological distance indicators. To further refine these relationships as well as understand their limitations, extensive data sets of high-precision light curves are required. At low redshift, multiple groups have answered the call, including the Calán/Tololo Supernova Survey with *BVRI* light curves of 29 SNe Ia (Hamuy et al. 1996), the Harvard–Smithsonian Center for Astrophysics (CfA) Supernova Group with >300 multiband light curves spread over four data releases (Riess et al. 1999; Jha et al. 2006; Hicken et al. 2009a, 2012; henceforth CfA1–4, respectively), the Carnegie Supernova Project (CSP) with >100 multiband light curves (Contreras et al. 2010; Folatelli et al. 2010; Stritzinger et al. 2011; Krisciunas et al. 2017; henceforth CSP1, CSP1a, CSP2, and CSP3, respectively), and our own Lick Observatory Supernova Search (LOSS) follow-up program with *BVRI* light curves of 165 SNe Ia (Ganeshalingam et al. 2010; henceforth G10). More recently, the Foundation Supernova Survey has published its first data release of 225 low-redshift SN Ia light curves derived from Pan-STARRS photometry (Foley et al. 2018). Despite these extensive campaigns, there exist many more well-observed light curves for high-redshift ($z \gtrsim 0.1$) SNe Ia than for those at low redshift (Betoule et al. 2014). As low-redshift SNe Ia are used to calibrate their high-redshift counterparts, a larger low-redshift sample will be useful for further improving width–luminosity relations, gauging systematic errors arising from the conversion of instrumental magnitudes to a uniform photometric system, and for investigating evolutionary effects over large time-scales.

The LOSS follow-up program has been in continuous operation for over 20 yr. The result is an extensive data base of SN Ia photometry from images obtained with the 0.76 m Katzman Automatic Imaging Telescope (KAIT) and the 1 m Nickel telescope, both located at Lick Observatory. G10 released SN Ia light curves from the first 10 yr of the LOSS follow-up campaign, and in this paper we publish the corresponding data set for the following 10 yr (2009–2018). We also include several earlier SNe Ia that were omitted from the first publication. In aggregate, our data set includes *BVRI* light curves of 93 SNe Ia with a typical cadence of $\sim$5.4 d drawn from a total of 21 441 images.

Our data set overlaps with those of CfA3, CfA4, and CSP3. In particular, we share 7 SNe with CfA3 and 16 SNe with CfA4; however, we expect the upcoming CfA5 release to have considerable overlap with ours, as it will be derived from observations over a similar temporal range. With regard to CSP3, we have 16 SNe in common. Accounting for overlaps, 28 SNe in our sample have been covered by at least one of these surveys, thus leaving 65 unique SNe in our sample.

The remainder of this paper is organized in the following manner. Section 2 details our data acquisition, including how our SNe are discovered and which facilities are employed to observe them. In Section 3, we discuss our data-reduction procedure, with particular emphasis placed on our automated photometry pipeline. Section 4 presents our results, including comparisons with those in the literature that were derived from the same KAIT and Nickel images, when such an overlap exists. We derive and discuss the properties of our light curves in Section 5, and our conclusions are given in Section 6.

2 OBSERVATIONS

2.1 Discovery

Many of the SNe Ia presented here were discovered and monitored by LOSS using the robotic KAIT (Li et al. 2000; Filippenko et al. 2001; see G10 for remarks on SN Ia discovery with LOSS). We note that the LOSS search strategy was modified in early 2011 to monitor fewer galaxies at a more rapid cadence, thus shifting focus to identifying very young SNe in nearby galaxies (e.g. Silverman et al. 2012a). Consequently, the proportion of our sample discovered by LOSS is less than that presented by G10. Those SNe in our sample that were not discovered with KAIT were sourced from announcements by other groups in the SN community, primarily in the form of notices from the Central Bureau of Electronic Telegrams (CBETs) and the International Astronomical Union Circulars (IAUCs). Whenever possible and needed, we spectroscopically classify and monitor newly discovered SNe Ia with the Kast double spectrograph (Miller & Stone 1993) on the 3 m Shane telescope at Lick Observatory. Discovery and classification references are provided for each SN in our sample in Table A1.

While the focus in this paper is on SNe Ia, we have also built up a collection of images containing SNe II and SNe Ib/c (see Filippenko 1997, for a discussion of SN spectroscopic classification). These additional data sets have been processed by our automated photometry pipeline and will be made publicly available pending analyses (de Jaeger et al. 2019; Zheng et al., in preparation, for the SN II and SN Ib/c data sets, respectively).

2.2 Telescopes

The images from which our data set is derived were collected using the 0.76 m KAIT ($\sim$86 per cent of the total) and the 1 m Nickel telescope ($\sim$14 per cent of the total), both of which are located at Lick Observatory on Mount Hamilton near San Jose, CA. The seeing at this location averages $\sim$2 arcsec, with some variation based on the season.

KAIT is a Ritchey–Chrétien telescope with a primary mirror focal ratio of *f*/8.2. Between 2001 September 11 and 2007 May 12, the CCD used by KAIT was an Apogee chip with 512 × 512 pixels, and henceforth it has been a Finger Lakes Instrument camera with the same number of pixels. We refer to these as KAIT3 and KAIT4, respectively.[1] Both CCDs have a scale of 0.8 arcsec pixel^{-1},

---

[1] G10 use KAIT1 and KAIT2 for earlier CCD/filter combinations. Our use of KAIT3 and KAIT4 is consistent with theirs.
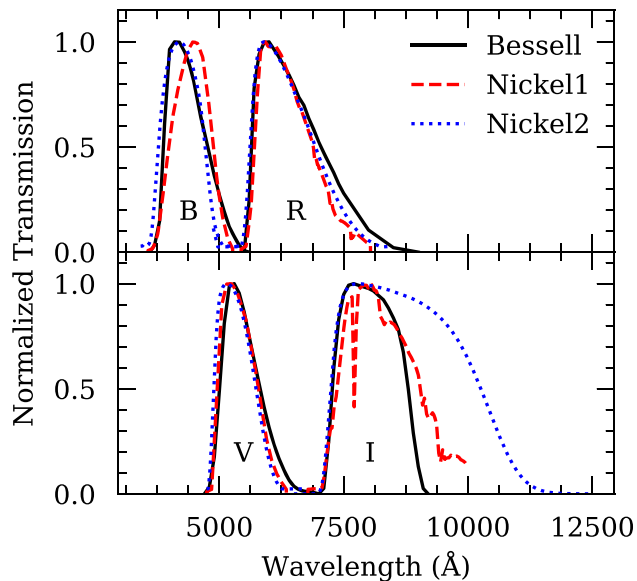
Figure 1. Transmission curves for the two Nickel 1 m configurations covered by our data set compared with standard Bessell (1990) *BVRI* curves.

yielding a field of view of 6.7 arcmin × 6.7 arcmin. As a fully robotic telescope, KAIT follows an automated nightly procedure to acquire data. Observations of a target are initiated by submitting a request file containing its coordinates as well as those of a guide star. A master scheduling program then determines when to perform the observations with minimal disruption to KAIT's SN search observations. Under standard conditions, we use an exposure time of 1–6 min in *B* and 1–5 min in each of *VRI*.

The 1 m Nickel is also a Ritchey–Chrétien telescope, but with a primary mirror focal ratio of *f*/5.3. Since 2001 April 3, its CCD has been a thinned, Loral, 2048 × 2048 pixel chip located at the *f*/17 Cassegrain focus of the telescope. With a scale of 0.184 arcsec pixel^{-1}, the field of view is 6.3 arcmin × 6.3 arcmin. In March of 2009, the filter set was replaced – we refer to the period before as Nickel1[2] and after as Nickel2. Pixels are binned by a factor of 2 to reduce readout time. Since 2006, most of our Nickel observations have been performed remotely from the University of California, Berkeley campus. Our observing campaign with Nickel is focused on monitoring more distant SNe and supplementing (particularly at late times) data taken with KAIT. Under standard conditions, we use exposure times similar to those for KAIT.

In Fig. 1, we compare the standard throughput curves of Bessell (1990) to those of the two Nickel 1 m configurations covered by our data set (G10 show the analogous curves for KAIT3 and KAIT4). We find good agreement between both Nickel1 and Nickel2 filter responses in the *VR* bands with the corresponding Bessell curves. In *B*, the agreement is good for Nickel2, but there is a noticeable discrepancy between the Nickel1 filter response compared to that of Bessell. The filter response in *I* for both Nickel configurations shows the most substantial departures from the Bessell standard, with Nickel2 exhibiting the most egregious disagreement. Nevertheless, the transmission curve has been verified through repeated measurements.

---

[2]Our Nickel1 is referred to as Nickel by G10.

3 DATA REDUCTION

With over 21 000 images spanning 93 SNe Ia with a median of 16 observed epochs, our data set is too large to manually process. We have therefore developed an automated photometry pipeline[3] to calculate light curves from minimally pre-processed[4] KAIT and Nickel images (those from other telescopes could be incorporated with minimal modifications). Although it makes use of distinct software packages and utilizes components written in several different programming languages, the pipeline is wrapped in a clean PYTHON interface. It automatically performs detailed logging, saves checkpoints of its progress, and can be run interactively if desired – thus, in cases where the data require special care, the user is able to perform each processing step manually with increased control. We detail the primary steps performed by the pipeline in the following sections.

3.1 Start-up and image checking

At a minimum, the pipeline requires four pieces of information to run: the coordinates of the target (right ascension and declination), the name of an image to use for selecting candidate calibration stars (henceforth, the 'reference image'), and a text file containing the name of each image to process. In the absence of additional information, the pipeline will make sensible assumptions in setting various parameters during the start-up process.

Processing commences by performing several checks on the specified images to see whether any should be excluded. The first removes any images collected through an undesired filter, and the second excludes those collected outside a certain range of dates. In processing our data set, we allow only unfiltered (referred to as 'Clear') images and those collected through standard *BVRI* filters between 60 d prior to and 2 yr after discovery as specified on the Transient Name Server (TNS),[5] to continue to subsequent processing steps.

3.2 Selection of calibration star candidates

In the next processing step, candidate calibration stars are identified in the reference image using a three-stage process. First, all sources above a certain threshold in the image are identified and those that are farther than 8 arcsec from that target are retained.

Next, a catalogue of potential calibration stars in the vicinity of the SN is downloaded (in order of preference) from the archives of Pan-STARRS (PS1; Chambers & Pan-STARRS Team 2018), the Sloan Digital Sky Survey (SDSS; Alam et al. 2015), or the AAVSO Photometric All-Sky Survey (APASS; Henden et al. 2018). The 40 brightest stars common to the reference image and the catalogue are then retained. If the pipeline is being run interactively, the user can visually inspect the positions of these stars against the reference image and remove any that should not be used (such as those that are not well separated from the target's host galaxy).

Finally, the magnitudes (and associated uncertainties) of the selected catalogue stars are converted to the Landolt system (Landolt 1983, 1992) using the appropriate prescription,[6] and subsequently

---

[3]https://github.com/benstahl92/LOSSPhotPypeline
[4]Pre-processing consists of removing bias and dark current, flat fielding, and determining an astrometric solution.
[5]https://wis-tns.weizmann.ac.il/
[6]The transformation given by Tonry et al. (2012) is used for PS1 catalogues, whereas SDSS and APASS catalogues are treated with the prescription of

Table 1. Summary of colour terms.

System	C_B	C_V	C_R	C_I
KAIT3	−0.057	0.032	0.064	−0.001
KAIT4	−0.134	0.051	0.107	0.014
Nickel1	−0.092	0.053	0.089	−0.044
Nickel2	0.042	0.082	0.092	−0.044

to the natural systems of the various telescope/CCD/filter sets that are spanned by our data set as discussed in Section 2.2. Conversion from the Landolt system to the aforementioned natural systems is accomplished using equations of the form

$$b = B + C_B(B - V) + \text{constant}, \tag{1a}$$

$$v = V + C_V(B - V) + \text{constant}, \tag{1b}$$

$$r = R + C_R(V - R) + \text{constant}, \tag{1c}$$

$$i = I + C_I(V - I) + \text{constant}, \tag{1d}$$

where lowercase letters represent magnitudes in the appropriate natural system, uppercase letters represent magnitudes in the Landolt system, and C_X is the linear colour term for filter X as given in Table 1. The KAIT3, KAIT4, and Nickel1 colour terms were originally given by G10, while those for Nickel2 are presented here for the first time. We derive the Nickel2 colour terms (and atmospheric correction terms, k_i; see Section 3.8.2) as the mean values of the appropriate terms measured over many nights using steps from the calibration pipeline described by G10.

3.3 Galaxy subtraction

A large proportion of SNe occur near or within bright regions of their host galaxies. It is therefore necessary to isolate the light of such an SN from that of its host prior to performing photometry. This is accomplished by subtracting the flux from the host at the position of the SN from the measured flux of the SN. To measure such host fluxes for the SNe in our sample needing galaxy subtraction (as determined by visual inspection and consideration of the offsets given in Table A1), we obtained template images using the 1 m Nickel telescope (for *BVRI* images) and KAIT (for unfiltered images) after the SNe had faded beyond detection, or from prior to the explosions if available in our data base. Template images selected for use in galaxy subtraction are pre-processed identically to science images as described earlier.

The first step in our subtraction procedure is to align each science image to its corresponding template image. We do this by warping each template such that the physical coordinates of its pixels match those of the science image. Next, we perform the subtraction using the ISIS package (Alard & Lupton 1998; Alard 2000), which automatically chooses stars in both images and uses them to compute the convolution kernel as a function of position. We use 10 stamps in the *x* and *y* directions to determine the spatial variation in the kernel. ISIS matches the seeing between the warped template image and the science image by convolving the one with better seeing and then subtracts the images. An example image with subtraction applied is shown in Fig. 2.
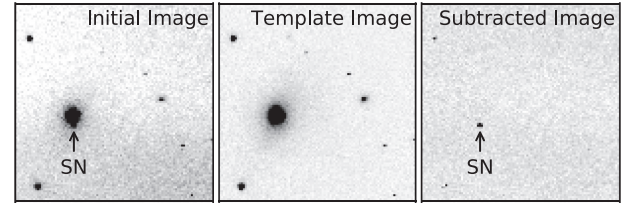
Robert Lupton in 2005 (https://www.sdss.org/dr12/algorithms/sdssUBVRITransform/).

Figure 2. Example of our galaxy-subtraction procedure. The left-hand image shows SN 2013gq on 2013 March 25 UT, with the SN flux clearly contaminated by the host galaxy. The centre image is the host-galaxy template used for subtraction, and the right-hand image is the result of our galaxy-subtraction procedure.

Some SNe in our data set occurred sufficiently far from the nuclei of their host galaxies to not suffer significant contamination from galaxy light. In these cases, we did not perform galaxy subtraction. Table A1 includes a column that indicates whether host-galaxy subtraction was performed for each SN in our sample.

3.4 Photometry

After galaxy subtraction has been performed (or skipped if not needed), the pipeline performs photometry on the target SN and each selected calibration star. For images that have been galaxy subtracted, photometry is only performed on the SN (as the calibration stars will have been subtracted out), and photometry of the calibration stars is measured from the unsubtracted images. This requires the user to take care when doing calibration (see Section 3.5) to ensure that the calibration stars used are not themselves contaminated by light from the SN's host galaxy.

By default, both point spread function (PSF) and aperture photometry (through multiple apertures), along with standard photometry uncertainty calculations for each, are performed using procedures from the IDL Astronomy User's Library.[7] Henceforth, we consider only PSF photometry.

The pipeline automatically keeps track of failures and removes the associated images from further processing. The user can easily track such failures and subsequently investigate each problematic image in more detail.

3.5 Calibration to natural systems

In the next step, the pipeline calibrates measured photometry to magnitudes in the appropriate natural system as follows. For each unsubtracted image, the mean magnitude of the selected calibration stars in the natural system appropriate to the image (from the catalogue downloaded and converted according to the specifications in Section 3.2) is computed. Next, the mean *measured* magnitude of the same set of reference stars is computed for each aperture. The difference between the former and the latter yields a set of offsets (one for each aperture) to add to the measured magnitudes such that, in the current image, the average magnitude of the selected calibration stars matches that from the catalogue. These offsets are also applied to the *measured* SN photometry from the image (and if it exists, the SN photometry from the associated galaxy-subtracted image). Standard techniques of error propagation are applied through these operations to determine the uncertainty in all

[7] https://idlastro.gsfc.nasa.gov/homepage.html

derived natural-system magnitudes, accounting for uncertainties in the calibration catalogue and photometry.

This procedure is clearly sensitive to which calibration stars are used, and so several steps are employed in an attempt to make an optimal decision. First, calibration is performed on each image using all available calibration stars. Any calibration stars that are successfully measured in <40 per cent of images are removed and calibration is run again using the remaining calibration stars. Next, any images in which <40 per cent of the calibration stars are successfully measured are removed from further consideration. After these two preliminary quality cuts are performed, an iterative process is used to refine and improve the calibration. Each iteration consists of a decision that changes which calibration stars are used or which images are included and a recalibration based on that decision.

When run interactively, the pipeline provides the user with extensive information to consider when making this decision. In each iteration, the reference image is displayed with the current calibration stars and the SN identified. It also provides tables for each passband that include, for each calibration star: the median measured and calibration magnitudes as well as the median of their differences, the standard deviation of the measured magnitudes, and the proportion of all images in the current passband for which the calibration star's magnitude was successfully measured. The user can remove certain calibration stars, or all that (in any passband) exceed a specific tolerance on the median magnitude difference. Other options and diagnostics are available, and thus an experienced user will develop certain decision-making patterns when performing interactive calibration, but further discussion is beyond the scope of this description.

The automated pipeline makes the decision as follows. Any image containing a reference star that differs by the greater of 3 standard deviations or 0.5 mag from the mean measured magnitude of that reference star in the relevant filter/system is removed and logged internally for later inspection. If no such discrepant images are identified, then the calibration star whose median difference between measured and reference magnitudes is most severe is removed, so long as the difference exceeds 0.05 mag. If neither of these two criteria is triggered, then the calibration process has converged and iteration exits successfully. However, if a point is reached where only two reference stars remain, the tolerance of 0.05 mag is incremented up by 0.05 mag and iteration continues. If the tolerance is incremented beyond 0.2 mag without iteration ending successfully, the calibration process exits with a warning.

The process described earlier tends to lead to robust results, but it is still possible for individual measurements to be afflicted by biases. Because of this, we visually inspect our results after automated calibration and in some cases interactively recalibrate and/or remove certain images if they are suspected of contamination or are of poor quality.

3.6 Landolt system light curves

The final stage of processing involves collecting each calibrated (natural system) magnitude measurement of the SN under consideration to form light curves (one for each combination of aperture and telescope system). Prior to transforming to the Landolt system, several steps are applied to these 'raw' light curves. First, magnitudes in the *same* passbands that are temporally close (<0.4 d apart) are averaged together. Next, magnitudes in *distinct* passbands that are similarly close in temporal proximity are grouped together so that they all have an epoch assigned as the average of their

individual epochs. These steps result in a light curve for each telescope system used in observations, with magnitudes in the associated natural system.

Next, these light curves are transformed to the Landolt system by inverting the equations of Section 3.2 and using the appropriate colour terms from Table 1. Finally, the transformed light curves are combined into a final, standardized light curve that represents all observations of the SN.

3.7 Uncertainties

To quantify the uncertainties in results derived from our processing routine, we inject artificial stars of the same magnitude and PSF as the SN in each image and then reprocess the images. We use a total of 30 artificial stars to surround the SN with five concentric, angularly offset hexagons of increasing size. The smallest has a 'radius' of ∼25 arcsec (exactly 20 KAIT pixels) and each concentric hexagon increases this by the same additive factor. We assign the scatter in the magnitudes of the 30 recovered artificial stars to be the uncertainty in our measurement of the SN magnitude. This is then added in quadrature with the calibration and photometry uncertainties and propagated through all subsequent operations, leading to the final light curve.

This method has the advantage of being an (almost) end-to-end check of our processing, and it can still be used effectively when certain steps (namely, host-galaxy subtraction) are not necessary. We note that by treating uncertainties in this way, we are making the assumption that the derived magnitude and PSF of the SN are correct. If this assumption is not met, the artificial stars we inject into each image will not be an accurate representation of the profile of the SN, and thus we cannot be assured that the distribution in their recovered magnitudes is a reasonable approximation to that of the SN. Furthermore, errors will be substantially overestimated when an injected star overlaps with a true star in the image. When this happens (as verified by a visual inspection), we do not inject a star at this position and thus in some cases the uncertainty estimate is made with slightly fewer than 30 stars.

Altogether, the final uncertainty on each magnitude in our light curves is derived by propagating three sources of uncertainty through our calculations. These sources are (i) 'statistical' (e.g. scatter in sky values, Poisson variations in observed brightness, uncertainty in sky brightness), (ii) 'calibration' (e.g. calibration catalogue, derived colour terms), and (iii) 'simulation' (as described in the preceding paragraphs). In terms of instrumental magnitudes, we find median uncertainties from these sources of 0.037, 0.015, and 0.062 mag, respectively. We show the distribution of each in Fig. 3.

3.8 Systematic errors

In order to combine or compare photometric data sets from different telescopes, one must understand and account for systematic errors. In this section, we consider sources of possible systematic errors and quantify their impact on our final photometry. As three of the four telescope/detector configurations spanned by our data set are already extensively considered by G10, our goal here is primarily to extend their findings to cover the fourth configuration, Nickel2.

3.8.1 Evolution of colour terms

The Nickel2 colour terms given in Table 1 are the average colour terms from observations of Landolt standards over many nights.
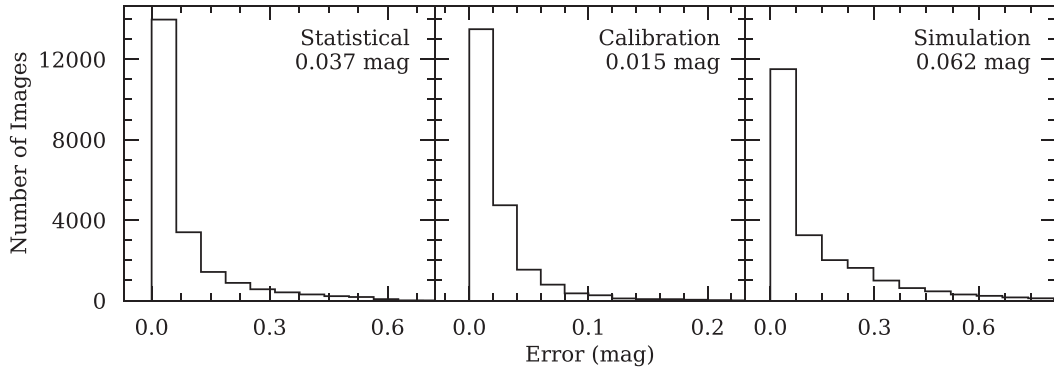
Figure 3. Distribution of uncertainties arising from statistical, calibration, and simulation sources. All magnitudes are instrumental magnitudes, and the median uncertainty from each source is printed.
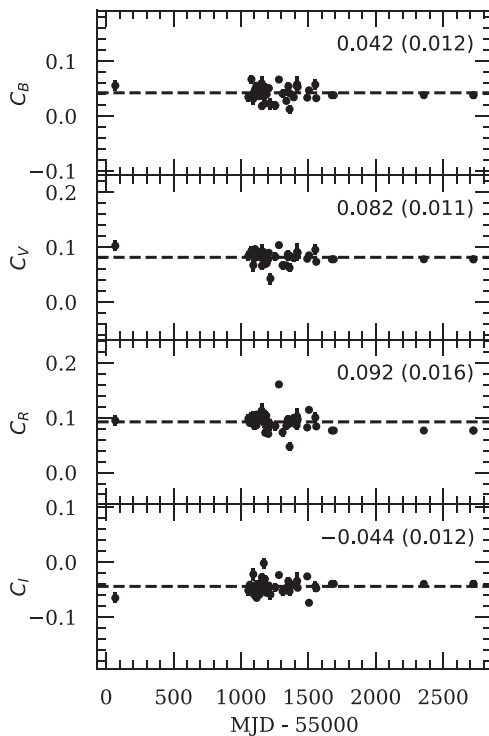
Figure 4. Nickel2 colour terms as a function of time. The mean and standard deviation in each passband are printed.

Figure 5. Same as Fig. 4, except for atmospheric correction terms used to transform Nickel2 natural-system magnitudes to the Landolt system.

Any evolution in the derived colour terms as a function of time introduces errors in the final photometry that are correlated with the colour of the SN and reference stars. To investigate this effect, we plot the Nickel2 colour terms as a function of time in Fig. 4, but find no significant evidence for temporal dependence. This conclusion is in line with the findings of G10 for KAIT3, KAIT4, and Nickel1.

3.8.2 Evolution of atmospheric terms

For the same set of nights for which we compute the colour terms that constitute Fig. 4, we also derive atmospheric correction terms. Because we source calibration stars from established catalogues (as

outlined in Section 3.2), our derived atmospheric correction terms affect processing only indirectly (i.e. in the determination of colour terms). As such, we discuss them here only as a stability check. Fig. 5 shows their evolution as a function of time. We do not find significant evidence for temporal dependence, which is consistent with the findings of G10 for KAIT3, KAIT4, and Nickel1. It is also worth noting that our derived terms ($k_B = 0.278$, $k_V = 0.157$, $k_R = 0.112$, and $k_I = 0.068$) are similar to those derived for Nickel1 by G10 (0.277, 0.171, 0.120, and 0.078, respectively).

3.8.3 Combining KAIT and Nickel observations

Another potential source of systematic error arises when combining observations from different configurations (e.g. KAIT4
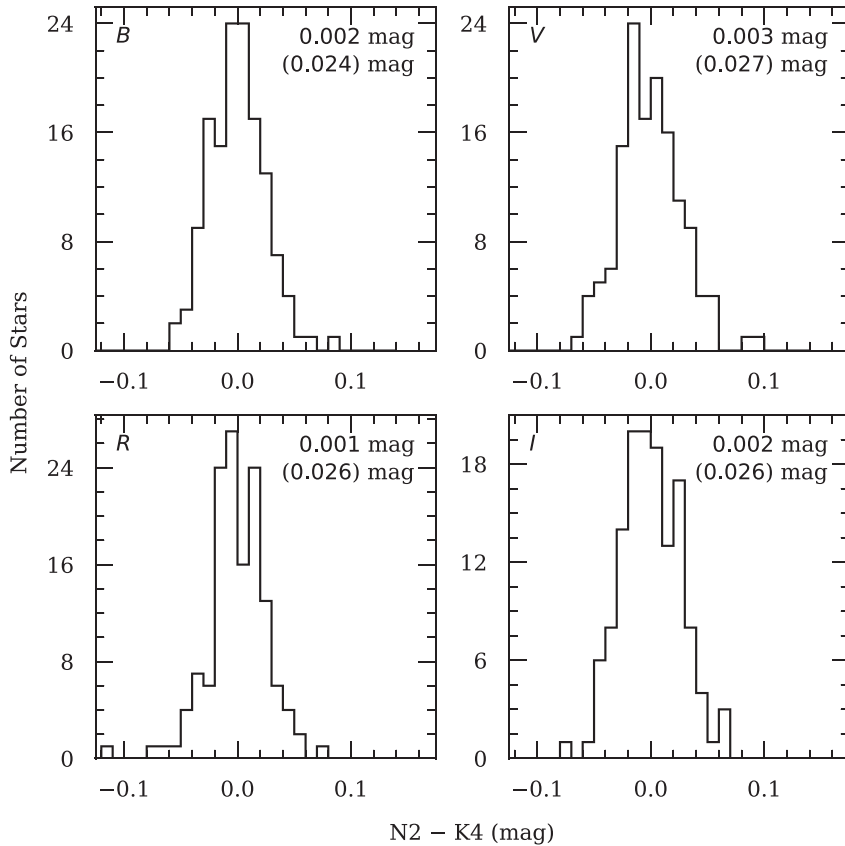
Figure 6. Distributions of the residuals of the mean derived magnitude of each calibration star used in determining final photometry for SNe in our data set covered by the KAIT4 and Nickel2 systems. The distributions reveal negligible offset between these two systems in all bands with a scatter <0.03 mag. The median and standard deviation of the residuals are printed for each passband.

and Nickel2). Any systematic differences between configurations introduce an error when observations from various systems are combined. To search for and investigate such differences, we compare the mean derived magnitude of each calibration star used in determining our final photometry for unique combinations of passband and system. In this investigation, we only consider instances where a calibration star was observed using two different systems. Fig. 6 shows the distribution of differences in each passband for the common set of calibration stars between the KAIT4 and Nickel2 systems, which have the largest overlap. Similar distributions were constructed for all other system combinations, and in all cases we find a median offset of $\lesssim 0.003$ mag[8] with scatter $\sigma \lesssim 0.03$ mag in each filter.

3.8.4 Galaxy subtraction

When subtracting host-galaxy light, the finite signal-to-noise ratio (S/N) of the images used as templates can limit measurements of the magnitude of an SN, thereby introducing a correlated error between epochs of photometry. To investigate the severity of this effect, G10 stacked images to obtain a deeper set of template images with increased S/N for SN 2000cn, an SN Ia from their sample. By

reprocessing their data with the new template images, G10 were able to probe the influence of host-galaxy templates derived from single images. Unsurprisingly, they found that the correlated error introduced by using a single image for a template is not negligible, but that it is appropriately accounted for by their error budget. As the modest differences between the Nickel1 and Nickel2 systems should not manifest any substantial differences with regard to galaxy subtraction in this manner, and because the error budget of G10 is similar to our own (as laid out in Section 3.7), we see no need for repetition of this test.

3.8.5 Total systematic error

Based on the preceding discussion, we assign a systematic uncertainty of 0.03 mag in *BVRI* to our sample, consistent with G10. This uncertainty is not explicitly included in our photometry tables or light-curve figures (e.g. Tables 2 and B3 and Fig. B1), but must be accounted for when combining our data set with others.

4 RESULTS

In this section, we present the results obtained by running our photometry pipeline on SNe Ia from LOSS images collected from 2009 through 2018, with several earlier SNe Ia also included. Basic information and references for each SN in our sample are provided

---

[8]The only exception is the median *I*-band offset between Nickel1 and KAIT3, which is 0.008 mag.

Table 2. Photometry of SN 2008ds.

SN	MJD	B (mag)	V (mag)	R (mag)	I (mag)	Clear (mag)	System
2008ds	54645.47	–	–	–	–	15.700 ± 0.033	KAIT4
2008ds	54646.47	–	–	–	–	15.574 ± 0.024	KAIT4
2008ds	54647.46	15.613 ± 0.012	15.630 ± 0.010	15.593 ± 0.012	15.744 ± 0.018	15.501 ± 0.010	KAIT4
2008ds	54650.47	15.503 ± 0.014	15.487 ± 0.010	15.475 ± 0.013	15.766 ± 0.016	–	KAIT4
2008ds	54653.13	15.483 ± 0.009	15.474 ± 0.005	15.413 ± 0.006	15.756 ± 0.008	–	Nickel1
2008ds	54653.44	15.492 ± 0.018	15.470 ± 0.010	15.435 ± 0.011	15.828 ± 0.017	–	KAIT4
2008ds	54655.13	15.570 ± 0.008	15.512 ± 0.006	15.451 ± 0.007	15.826 ± 0.009	–	Nickel1
2008ds	54655.48	15.567 ± 0.016	15.507 ± 0.012	15.467 ± 0.015	15.925 ± 0.023	–	KAIT4
2008ds	54658.13	15.704 ± 0.008	15.606 ± 0.006	15.542 ± 0.006	15.962 ± 0.008	–	Nickel1
2008ds	54662.16	15.995 ± 0.012	15.773 ± 0.005	–	–	–	Nickel1

Note. First 10 epochs of *BVRI* + unfiltered photometry of SN 2008ds. This table shows the form and content organization of a much larger table that covers each epoch of photometry for each SN in our data set. The full table is available in the online version of this article.

in Table A1. The NASA/IPAC Extragalactic Database (NED)[9] and the TNS were used to source many of the given properties.

Fig. B1 shows our light curves, each shifted such that time is measured relative to the time of maximum *B*-band brightness as determined by MLCS2K2 (Jha et al. 2007) fits or Gaussian process interpolations (Lochner et al. 2016) for peculiar SNe (see Sections 5.2.2 and 5.1, respectively). An example of our photometry is given in Table 2. In addition to leaving out the systematic 0.03 mag uncertainty derived in Section 3.8.5, we choose to provide light curves without considering corrections such as Milky Way (MW) extinction, *K*-corrections (Oke & Sandage 1968; Hamuy et al. 1993; Kim, Goobar & Perlmutter 1996), or *S*-corrections (Stritzinger et al. 2002). This provides future studies the opportunity to decide which corrections to apply and full control over how they are applied. Because of the low-redshift range of our data set (see the right-hand panel of Fig. 7) and the similarity between systems, the *K*- and *S*-corrections will be quite small in any case. Though magnitudes in Fig. B1 and Table 2 are given in the Landolt system, we also make our data set available in natural-system magnitudes for those that would benefit from the reduced uncertainties (see Appendix B2). Our entire photometric data set (Landolt and natural-system magnitudes) is available online from the Berkeley SuperNova DataBase[10] (SNDB; Silverman et al. 2012b; Shivvers et al. 2016).

4.1 The LOSS sample

In order to accurately measure and exploit the correlation between light-curve width and luminosity for SNe Ia, thus allowing for precision measurements of cosmological parameters, densely sampled multicolour light curves that span pre- through post-maximum evolution are required. In Fig. 8, we show the number of epochs of photometry for each SN in our sample versus the average cadence between epochs of photometry. The plot indicates that the majority of SNe in our sample have more than 10 epochs of observations with a cadence of fewer than 10 d, while a significant number of SNe were observed many more times at even higher frequency. These metrics confirm that, on average, our light curves are well sampled and span a large range of photometric evolution.

The left-hand panel of Fig. 7 presents a histogram of the total number of photometry epochs for all SNe in our sample, and we find a median of 16 epochs. SN 2011dz has just 1 epoch of photometry and five objects (SNe 2006ev, 2009D, 2009hp, 2012E, 2012bh) have 2 epochs each, while SN 2013dy has 126 (the most), followed by SN 2012cg and then SN 2017fgc. We begin photometric follow-up observations for the typical SN in our sample ~4.6 d before maximum light in the *B* band, with 52 SNe having data before maximum brightness. The centre panel of Fig. 7 shows the distribution of first-observation epochs for our sample. The median redshift of our full sample is 0.0192, with a low of 0.0007 (SN 2014J) and a high of 0.0820 (SN 2017dws). We show the distribution of redshifts in the right-hand panel of Fig. 7. If we restrict to $z \geq 0.01$ (i.e. within the Hubble flow), our sample consists of 71 SNe with a median redshift of 0.0236.

4.2 Comparison with published LOSS reductions

For several of the SNe presented here, previous reductions of the photometry (usually performed with an earlier photometry pipeline, developed by G10) have been published. A comparison between these previous results and our own offers a useful efficacy check of our pipeline while avoiding the issues arising from comparisons between different telescopes or photometric systems. Wherever sufficient overlap between one of our light curves and that from a previous publication exists, we quantify the extent to which the data sets agree by computing the weighted mean residual. In some cases, we further compare by considering the agreement between derived quantities such as the light-curve shape, $\Delta m_{15}(B)$, and the time of maximum brightness, $t_{B_{max}}$. We emphasize that in general our results are derived from different sets of reference stars for calibration than those used to derive the results with which we compare, and that even when reference stars overlap, we may draw their magnitudes from different catalogues.

4.2.1 SN 2005hk

Phillips et al. (2007) published optical light curves from KAIT data for the Type Iax SN 2005hk. At the time of publication, no template images were available and so the authors acknowledged that their derived magnitudes for the SN, located ~18.5 arcsec from the nucleus of its host galaxy, were probably affected by the background light. In the prevailing time, we have obtained template images of the host and used them to separate its flux from that of the SN. Comparing results, both of which were obtained using PSF-fitting
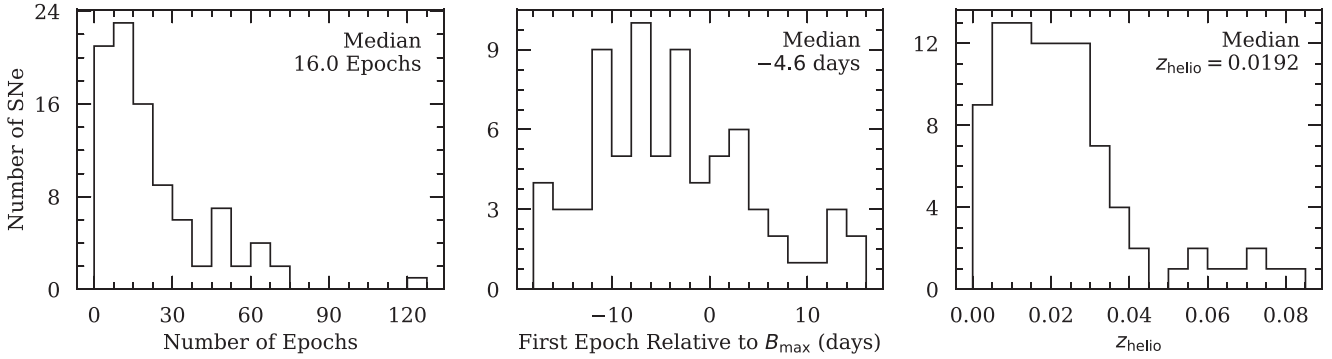
Figure 7. Distributions of data set parameters. The left-hand panel is the number of epochs of photometry as measured from *V*-band observations, the centre panel is the first epoch of observation relative to time of maximum *B*-band light, and the right-hand panel is redshift.
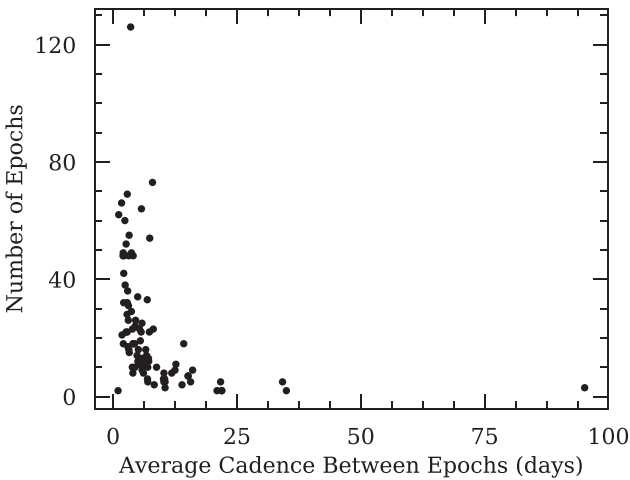
Figure 8. Scatterplot of the number of photometry epochs for each SN versus the average cadence between epochs. The tight grouping with a lower average cadence and mid to high number of epochs indicates that our SNe are well sampled and cover a large portion of photometric evolution. The single SN with an average cadence in excess of 80 d is SN 2016ffh.

photometry, we find agreement to within 0.090 mag in *BVRI*. It is worth noting that our measurements are generally fainter, especially when the SN is rising and declining. This suggests that host-galaxy subtraction is indeed necessary for this object. We also compare measurements of the light-curve shape parameter $\Delta m_{15}(B)$, and find strong agreement between our value (see Section 5.1 and Table B1) of 1.58 ± 0.05 mag and theirs of 1.56 ± 0.09 mag.

4.2.2 SN 2009dc

Our Nickel and KAIT images of the extremely slow-evolving SN 2009dc – a super-Chandrasekhar candidate (see Noebauer et al. 2016, for a summary of the properties of this subclass of thermonuclear SNe) – were initially processed and used to construct light curves by Silverman et al. (2011). In both our reduction and theirs, PSF-fitting photometry was employed and galaxy subtraction was not performed owing to the large separation between the SN and its host galaxy. We find agreement to better that 0.020 mag in *BVRI*. Furthermore, we derive $\Delta m_{15}(B) = 0.71 \pm 0.06$ mag, consistent with their result of $\Delta m_{15}(B) = 0.72 \pm 0.03$ mag.

4.2.3 SN 2009ig

Optical light curves of SN 2009ig were derived from KAIT data and published by Foley et al. (2012). Both our reduction procedure and theirs used PSF-fitting photometry after subtracting template images of the host galaxy. We find that our results agree to within 0.055 mag in *BVRI*. It is worth adding that SN 2009ig is in a field with very few stars available for comparison when calibrating to natural-system magnitudes – Foley et al. (2012) used only one star for comparison while we have used two. In light of these challenges, we are content with the similarity between our results, especially because we obtain a consistent value of $\Delta m_{15}(B)$.[11] As an added check, we reprocessed our data for SN 2009ig using the same calibration star as Foley et al. (2012) and find agreement to within ∼0.025 mag in *BVRI*.

4.2.4 SN 2011by

KAIT *BVRI* photometry of SN 2011by was published by Silverman, Ganeshalingam & Filippenko (2013) and later studied in detail by Graham et al. (2015). In comparing our light curves (which have host-galaxy light subtracted) to theirs (which do not), we find agreement to within ∼0.05 mag. Furthermore, Silverman et al. (2013) found $B_{max} = 12.89 \pm 0.03$ mag and $\Delta m_{15}(B) = 1.14 \pm 0.03$ mag, which are consistent with our results of $B_{max} = 12.91 \pm 0.02$ mag and $\Delta m_{15}(B) = 1.09 \pm 0.10$ mag.

4.2.5 SN 2011fe

SN 2011fe/PTF11kly in M101 is perhaps the most extensively observed SN Ia to date (Nugent et al. 2011; Richmond & Smith 2012; Vinkó et al. 2012; Graham et al. 2015; Zhang et al. 2016). Photometry derived from KAIT data has been published by Graham et al. (2015) and Zhang et al. (2016), but we compare only with the latter. For the 20 epochs that overlap between our data set and theirs, we find agreement of better than ∼0.04 mag in *BVRI*.

4.2.6 SN 2012cg

SN 2012cg was discovered very young by LOSS, and KAIT photometry from the first ∼2.5 weeks following discovery was

---

[11]We find $\Delta m_{15}(B) = 0.85 \pm 0.12$ mag (the large uncertainty is mostly due to the uncertainty in the time of *B* maximum), while Foley et al. (2012) find $\Delta m_{15}(B) = 0.89 \pm 0.02$ mag.

published by Silverman et al. (2012a). Because of the small temporal overlap between this early-time data set and the much more expansive set presented herein, and because we have obtained template images and used them to remove the host-galaxy light, it is not instructive to quantitatively compare between our data set and theirs. We note, however, that we find a similar time of *B*-band maximum and that there is clear qualitative agreement between the two samples.

4.2.7 SN 2013dy

Zheng et al. (2013) published early-time KAIT photometry of SN 2013dy and used it to constrain the first-light time, while Pan et al. (2015) published extensive optical light curves. We compare the 85 overlapping epochs of our data set with those of Pan et al. (2015), both of which were obtained using PSF-fitting photometry, and find agreement better than ∼0.03 mag in *BVRI*.

4.2.8 SN 2013gy

KAIT *B* and *V* observations were averaged in flux space to create so-called *BV*.5-band photometry by Holmbo et al. (2019), who then used *S*-corrections to transform to the *g* band on the Pan-STARRS1 photometric system. Because of the difference between our choice of photometric system and theirs, we opt only to compare derived light-curve properties. Our result for the time of *B*-band maximum is within 1 d of theirs (consistent, given the uncertainties), and we find $\Delta m_{15}(B) = 1.247 \pm 0.072$ mag, nearly identical to their result of $\Delta m_{15}(B) = 1.234 \pm 0.060$ mag.

4.2.9 SN 2014J

SN 2014J in M82 has been extensively studied – unfiltered KAIT images were presented by Zheng et al. (2014) and used to constrain the explosion time, and Foley et al. (2014) published photometry from many sources, including a number of KAIT *BVRI* epochs. A comparison between our results and theirs reveals substantial (∼0.2 mag) discrepancies. The origin of this disagreement stems from differences in our processing techniques – Foley et al. (2014) calibrated instrumental magnitudes against reference-star magnitudes *in the Landolt system* (thereby disregarding linear colour terms), while we have done calibrations with reference-star magnitudes *in the natural system* appropriate to the equipment before transforming to the Landolt system. When we reprocess our data using the former approach in conjunction with the reference stars used by Foley et al. (2014), we find agreement between our non-host-galaxy subtracted light curve and theirs to within 0.01 mag in *BVRI*. Our final light curve for SN 2014J reflects the latter approach (which is the default of our pipeline), and was derived using a different set of calibration stars after subtracting host-galaxy light.

4.2.10 SN 2016coj

SN 2016coj was discovered at a very early phase by LOSS, and Zheng et al. (2017) presented the first 40 d of our optical photometric, low- and high-resolution spectroscopic, and spectropolarimetric follow-up observations. Because our full photometric data set encompasses a much broader time frame and Zheng et al. (2017) focused only on unfiltered photometry, a direct comparison is not possible. However, we note that our derived $\Delta m_{15}(B) = 1.33 \pm 0.03$ mag, $B_{max} = 13.08 \pm 0.01$ mag, and

$t_{B_{max}} = 57547.15 \pm 0.19$ MJD are consistent with their preliminary reporting, based on photometry *without* host-galaxy subtraction, of 1.25 ± 0.12 mag, 13.1 ± 0.1 mag, and 57547.35 MJD, respectively.

4.2.11 Summary of comparisons

We have compared the results of our photometry to the results derived from previous processing pipelines used by our group for 10 SNe Ia. Of these, five (SNe 2009dc, 2009ig, 2011fe, 2013dy, and 2014J) can be directly compared in the sense that identical processing steps (e.g. whether galaxy subtraction was performed) were used. For this subsample, we find excellent (≲0.05 mag) agreement except for the cases of SN 2009ig (<0.055 mag) and SN 2014J (∼0.2 mag). However, we are able to attain much stronger agreement (≲0.025 and ≲0.010 mag, respectively) if we employ the same calibration procedures used in the original processing. For the remaining five, we find consistent results in derived light-curve parameters, and more generally, good qualitative agreement in the shape of the light curves.

5 DISCUSSION

The absolute peak brightness that an SN Ia attains has been shown to be strongly correlated with the 'width' of its light curve (e.g. Phillips 1993). Thus, given a model for this correlation and a measurement of the light-curve width of an SN Ia, one can compute its intrinsic peak luminosity. By comparing this to its *observed* peak brightness, the distance to the SN Ia can be estimated. In this section, we examine the properties of the light curves in our sample in more detail. Specifically, in Section 5.1 we directly measure light-curve properties from interpolations, whereas in Section 5.2 we model our light curves with light-curve fitting tools.

5.1 Interpolated light-curve properties

Perhaps the most ubiquitous parametrization of the width (or decline rate) of an SN Ia light curve is $\Delta m_{15}(X)$, the difference in its magnitude at maximum light and 15 d later in passband *X*. We measure this quantity in *B* and *V* by interpolating the (filtered) light curves using Gaussian processes, a technique that has proved useful in astronomical time-series analysis due to its incorporation of uncertainty information and robustness to noisy or sparse data (Lochner et al. 2016).

For each SN in our sample where the photometry in *B* and/or *V* encompasses the maximum brightness in that band, we employ the following approach using tools from the SNOOPY[12] package (Burns et al. 2011). First, we interpolate the light curve in each passband using Gaussian processes, allowing us to determine the time at which that light curve peaks. With the phase information that this affords, the data are *K*-corrected using the spectral energy distribution (SED) templates of Hsiao et al. (2007). We further correct the data for MW extinction (Schlafly & Finkbeiner 2011) and then perform a second interpolation on the corrected data. From this interpolation, we measure $t_{X_{max}}$, X_{max}, and $\Delta m_{15}(X)$ – the time of maximum brightness, maximum apparent magnitude, and light-curve width parameter, respectively – in filters *B* and *V*. In measuring $\Delta m_{15}(X)$, we correct for the effect of time dilation. The final results of this fitting process are presented in Table B1.

[12] https://csp.obs.carnegiescience.edu/data/snpy/documentation/snoopy-manual-pdf

5.2 Applying light-curve fitters

While interpolation is viable for well-sampled light curves, those that are more sparsely sampled or that do not unambiguously constrain the maximum brightness cannot be reliably treated with this technique. Furthermore, interpolation completely disregards the effects of host-galaxy extinction, which must be accounted for when estimating distances.

Because of these limitations, we also employ two light-curve fitters to measure the properties of our sample. To the extent that the templates used by these fitters span the diversity in our data set, this approach does not suffer from the same limitations as interpolation.

5.2.1 SNOOPY $E(B − V)$ model

We use the so-called EBV_model in SNOOPY to simultaneously fit the *BVRI* light curves in our sample. In observed band *X* and SN rest-frame band *Y*, the model takes on the mathematical form

$$\begin{aligned}
m_X(t − t_{max}) = \ & T_Y(t_{rel}, \Delta m_{15}) + M_Y(\Delta m_{15}) + \mu \\
& + R_X E(B − V)_{gal} + R_Y E(B − V)_{host} \\
& + K_{X,Y}\left(z, t_{rel}, E(B − V)_{host}, E(B − V)_{gal}\right), \quad (2)
\end{aligned}$$

where *m* is the observed magnitude, t_{max} is the time of *B*-band maximum, $t_{rel} = (t' − t_{max})/(1 + z)$ is the rest-frame phase, *M* is the rest-frame absolute magnitude of the SN, μ is the distance modulus, $E(B − V)_{gal}$ and $E(B − V)_{host}$ are the reddening due to the Galactic foreground and host galaxy, respectively, *R* is the total-to-selective absorption, and *K* is the *K*-correction (which depends on the epoch and can depend on the host and Galactic extinction).

SNOOPY generates the template, $T(t, \Delta m_{15})$, from the prescription of Prieto, Rest & Suntzeff (2006). As indicated, the light curve is parameterized by the decline-rate parameter, Δm_{15}, which is similar to $\Delta m_{15}(B)$. It is important to note, however, that these quantities are *not* identical, and may deviate from one another randomly and systematically (see section 3.4.2 in Burns et al. 2011). The model assumes a peak *B*-band magnitude and *B* − *X* colours based on the value of Δm_{15}, with six possible calibrations derived from CSP1a. We use calibration #6, which is derived from the best-observed SNe in the sample, less those that are heavily extinguished.

The template-fitting process with SNOOPY consists of the following steps. First, an initial fit is made to determine the time of *B*-band maximum. This allows for initial *K*-corrections to be determined using the SED templates from Hsiao et al. (2007). The *K*-corrected data are then fit again, allowing colours to be computed as a function of time. Next, improved *K*-corrections are computed, warping the SED such that it matches the observed colours. Last, a final fit is performed using the improved *K*-corrections. The results from fitting are t_{max}, Δm_{15}, $E(B − V)_{host}$, and μ. We present these quantities for our data set in Table B2. We also visualize the distributions of Δm_{15} and $E(B − V)_{host}$ from our data set in Fig. 9, with the corresponding distributions from Burns et al. (2011) overlaid for comparison.

For Δm_{15}, we find a median value of 1.11 mag with a standard deviation of 0.26 mag, consistent with the respective values of 1.15 and 0.32 mag from the data set of Burns et al. (2011). For $E(B − V)_{host}$, we find a median of 0.10 mag with a dispersion of 0.29 mag for our sample, similar to their values of 0.12 and 0.29 mag, respectively. We stress that comparing these parameters between our data set and that of Burns et al. (2011) is only to provide a diagnostic view of how our sample is distributed relative to another from the literature – there is minimal overlap between the two samples, so we are *not* looking for a one-to-one correspondence.

Furthermore, we can use the fitted model for each light curve to calculate other parameters of interest, such as those derived from direct interpolation. This gives a method by which we can check for consistency in our results. For example, we expect the time of maximum brightness in a given band to be the same, regardless of whether it was calculated from an interpolation or a fitted model. We employ Kolmogorov–Smirnoff tests on our calculated times of maximum (where we have results from both interpolation and template fitting) to quantify the likelihood that those from interpolation are drawn from the same distribution as those from template fitting. In both cases ($t_{B_{max}}$ and $t_{V_{max}}$), we find *P*-values of unity, indicating that our expectation is met.

Applying such tests for B_{max} and V_{max} is less straightforward because of the presence of systematic offsets between results derived from interpolation and those derived from fitting SNOOPY $E(B − V)$ model. While both methods provide peak magnitudes after performing *K*-corrections and correcting for MW reddening, only
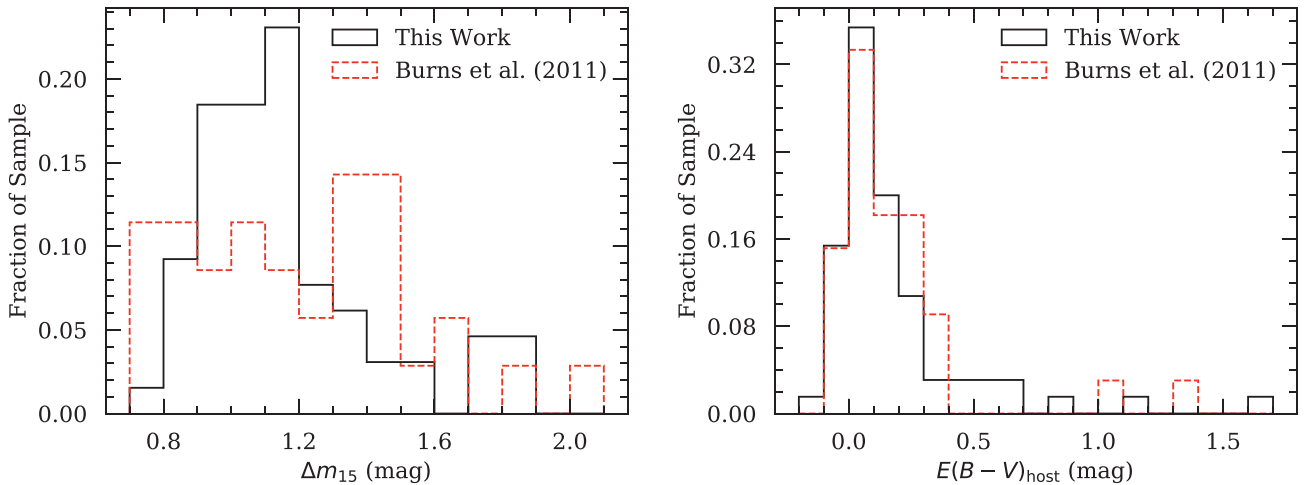

Figure 9. Distributions of Δm_{15} and $E(B − V)_{host}$ from SNOOPY $E(B − V)$ model fits to the light curves in our data set appear in black. We include the corresponding distributions derived from Burns et al. (2011) in red.
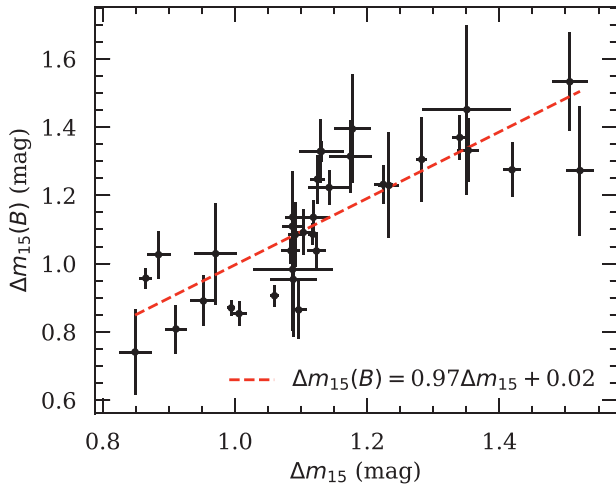
Figure 10. Comparison of the decline-rate parameter as measured from our Gaussian process interpolations, $\Delta m_{15}(B)$, with that obtained directly from our SNOOPY $E(B-V)$ model fits, Δm_{15}.

the $E(B-V)$ model fits account for host-galaxy reddening. With this caveat noted, it is still instructive to make comparisons, and in doing so we find P-values of 0.708 and 0.981 for B_{max} and V_{max}, respectively. If we impose restrictions to make the comparison more legitimate – namely, to use only those SNe in our sample that are not heavily extinguished by their hosts ($|E(B-V)_{host}| < 0.1$ mag), that are spectroscopically normal (as given in Table A1), and for which SNOOPY measures $\Delta m_{15} < 1.7$ mag – we find substantially improved agreement, with P-values of 0.956 and 1.000, respectively.

As noted earlier, Δm_{15} does not exactly correspond to $\Delta m_{15}(B)$. In comparing them, Burns et al. (2011) found a linear relationship of $\Delta m_{15}(B) = 0.89\Delta m_{15} + 0.13$. Performing an analogous comparison with our data set subjected to the aforementioned light-curve shape restriction, we find $\Delta m_{15}(B) = (0.97 \pm 0.12)\Delta m_{15} + (0.02 \pm 0.14)$. Fig. 10 shows our derived linear relationship within the context of our data.

5.2.2 MLCS2K2

In addition to the methods described earlier, we have run MLCS2K2.v007 (Jha et al. 2007) on our sample of light curves. MLCS2K2 parameterizes the absolute magnitude of an SN in terms of Δ, which quantifies how luminous an SN is relative to a fiducial value. By using a quadratic dependence on Δ, intrinsic variations in peak magnitude are modelled without introducing a parameter for intrinsic colour. In order to do this, MLCS2K2 corrects for MW reddening and *attempts* to correct for reddening due to the host galaxy by employing a reddening law, R_V, to obtain the host-galaxy extinction parameter, A_V, after employing a prior on $E(B-V)$.

MLCS2K2 yields four fitted parameters for each *BVRI* light curve: the distance modulus (μ), the shape/luminosity parameter (Δ), the time of B-band maximum (t_0), and the host-galaxy extinction parameter (A_V). In running MLCS2K2 on our data set, we fix R_V to 1.7 and use the default host-reddening prior, which consists of a one-sided exponential with scale length $\tau_{E(B-V)} = 0.138$ mag. We use the SED templates of Hsiao et al. (2007), and following Hicken et al. (2009b) we use MLCS2K2 model light curves trained using $R_V = 1.9$. We present the results of running MLCS2K2.v007 on our sample in Table B2 and the distributions of Δ and A_V in Fig. 11.

We find a median and standard deviation for Δ of -0.11 and 0.46, and for A_V of 0.20 and 0.45. Comparing these to the corresponding parameters from CfA3, we find reasonable agreement, with -0.04 and 0.48, and 0.13 and 0.44, respectively. Our data set only shares minimal overlap with that of CfA3, so these comparisons serve to reveal how our data set is distributed relative to another low-z sample.

5.3 Comparison of light-curve fitter results

To make any cosmological statements based on the results in the previous section is beyond the scope of this paper, as this would require a detailed study and justification of the utilized light-curve fitters and their parameters, among many other considerations. It is interesting and possible, however, to compare results from the two light-curve fitters we employ to check for consistency. As the principal quantity of interest when fitting the light curves of SNe Ia is distance, we will focus our comparison on the derived distance moduli.

The left-hand plot in Fig. 12 compares the distance moduli from SNOOPY and MLCS2K2 after correcting to put the measurements on the same scale (so that *relative* distance moduli are compared, independent from assumptions about the Hubble constant). This correction consists of adding an offset to the distance moduli from each fitter such that the value of H_0 measured from each set of results yields 65 km s^{-1} Mpc^{-1}. We perform this comparison only for spectroscopically normal SNe Ia in our sample for which SNOOPY finds $\Delta m_{15} < 1.7$ mag and for which $z > 0.01$. Of course, further restrictions should be placed when selecting a sample for cosmological purposes, but our selection is reasonable for performing a general comparison. We find strong agreement between the two sets of corrected distance moduli – a Kolmogorov–Smirnoff test gives a P-value of 1.000. The median residual is -0.026 mag with a statistical dispersion of 0.135 mag.

If we were to ensure consistency in choosing the parameters for each light-curve fitter, the residuals would almost certainly decrease. In particular, when fitting with MLCS2K2, we place an exponentially decaying prior on A_V, but no such prior was imposed with SNOOPY. This difference may well manifest in statistically and systematically different results for host-galaxy reddening and distance moduli between the two fitters. We compare host-galaxy reddening results in the right-hand panel of Fig. 12, where for MLCS2K2 we have converted to reddening using $E(B-V)_{host} = A_V/R_V$, with $R_V = 1.7$. The agreement is reasonable, with a median residual of -0.056 mag and statistical uncertainty of 0.055 mag. Furthermore, the facts that the median residual (SNOOPY minus MLCS2K2) is negative and that the disagreement is most severe for small $E(B-V)_{host}$ are consistent with what one might expect given the prior imposed by MLCS2K2.

6 CONCLUSION

In this paper, we present *BVRI* (along with some unfiltered) light curves of 93 SNe Ia derived from images collected by the LOSS follow-up program primarily over the interval from 2009 to 2018, but with several instances as early as 2005. Careful and consistent observational and processing techniques ensure that our data are prepared in a homogeneous fashion. We estimate the systematic uncertainty in our data set to be 0.03 mag in *BVRI*, and we encourage the community to incorporate our light curves in future studies.

In cases where our results overlap with previous reductions of LOSS data, we provide a set of comparisons as a consistency check. In general, we find good agreement, giving us confidence in the
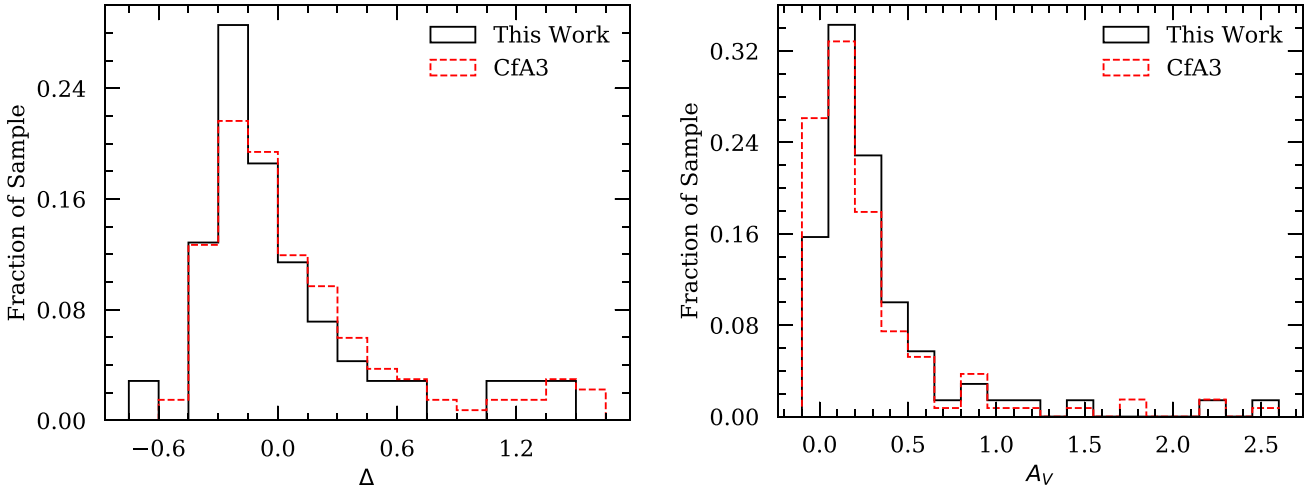
Figure 11. Distributions of Δ and A_V from MLCS2K2 model fits to the light curves in our data set appear in black. We include the corresponding distributions derived from CfA3 in red.
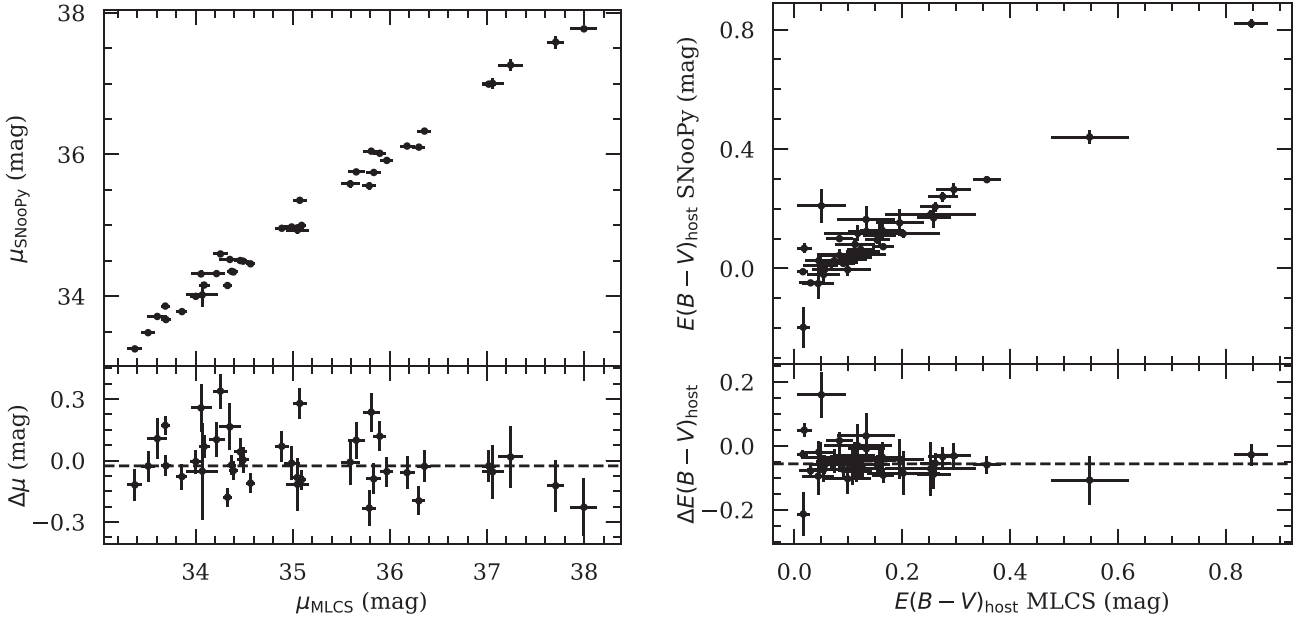

Figure 12. Comparison of the (scaled) distance modulus and host-galaxy reddening results from both light-curve fitters for the selected subset of our data set.

quality of our processing and analysis. When combined with the light curves of G10, the resulting data set spans 20 yr of observations of 258 SNe Ia from the same two telescopes.

We study the properties of the light curves in our data set, with particular focus on the parameters used in various width–luminosity relationships. Using direct interpolations, we measured $\Delta m_{15}(B)$ and $\Delta m_{15}(V)$. We also apply the light-curve fitters SNOOPY and MLCS2K2.v007 to measure Δm_{15} and Δ, respectively. We compare results derived from these methods, and find an acceptable degree of agreement given the differences in starting assumptions.

A consideration of the photometric data set presented here alongside spectra from the Berkeley Supernova Ia Program (BSNIP) data base will enable further utility. Our data set overlaps with 13 SNe from the first BSNIP data release (Silverman et al. 2012b), with an average of 4.5 spectra each. Furthermore, we expect significant

overlap between the SNe in our data set and our upcoming second BSNIP data release of ∼700 spectra from ∼250 SNe Ia observed over a similar temporal range (Stahl et al., submitted).

ACKNOWLEDGEMENTS

REFERENCES

Alam S. et al., 2015, ApJS, 219, 12
Alard C., 2000, A&AS, 144, 363
Alard C., Lupton R. H., 1998, ApJ, 503, 325
Bessell M. S., 1990, PASP, 102, 1181
Betoule M. et al., 2014, A&A, 568, A22
Burns C. R. et al., 2011, AJ, 141, 19
Chambers K., Pan-STARRS Team, 2018, American Astronomical Society Meeting Abstracts #231, 102.01
Contreras C. et al., 2010, AJ, 139, 519
de Jaeger T. et al., 2019, MNRAS, 00, 00
Filippenko A. V., 1997, ARA&A, 35, 309
Filippenko A. V. et al., 1992a, ApJ, 384, L15
Filippenko A. V. et al., 1992b, AJ, 104, 1543
Filippenko A. V., Li W. D., Treffers R. R., Modjaz M., 2001, in Paczynski B., Chen W.-P., Lemme C., eds, ASP Conf. Ser. Vol. 246, IAU Colloq. 183: Small Telescope Astronomy on Global Scales. Astron. Soc. Pac., San Francisco, p. 121
Folatelli G. et al., 2010, AJ, 139, 120
Foley R. J. et al., 2012, ApJ, 744, 38
Foley R. J. et al., 2013, ApJ, 767, 57
Foley R. J. et al., 2014, MNRAS, 443, 2887
Foley R. J. et al., 2018, MNRAS, 475, 193
Ganeshalingam M. et al., 2010, ApJS, 190, 418 (G10)
Ganeshalingam M., Li W., Filippenko A. V., 2013, MNRAS, 433, 2240
Graham M. L. et al., 2015, MNRAS, 446, 2073
Hamuy M., Phillips M. M., Wells L. A., Maza J., 1993, PASP, 105, 787
Hamuy M. et al., 1996, AJ, 112, 2408
Henden A. A., Levine S., Terrell D., Welch D. L., Munari U., Kloppenborg B. K., 2018, American Astronomical Society Meeting Abstracts #232, 223.06
Hicken M. et al., 2009a, ApJ, 700, 331
Hicken M., Wood-Vasey W. M., Blondin S., Challis P., Jha S., Kelly P. L., Rest A., Kirshner R. P., 2009b, ApJ, 700, 1097
Hicken M. et al., 2012, ApJS, 200, 12
Holmbo S. et al., 2019, A&A, 627, A174
Hsiao E. Y., Conley A., Howell D. A., Sullivan M., Pritchet C. J., Carlberg R. G., Nugent P. E., Phillips M. M., 2007, ApJ, 663, 1187
Jha S. et al., 2006, AJ, 131, 527
Jha S., Riess A. G., Kirshner R. P., 2007, ApJ, 659, 122
Kasen D., Woosley S. E., 2007, ApJ, 656, 661
Kim A., Goobar A., Perlmutter S., 1996, PASP, 108, 190
Krisciunas K. et al., 2017, AJ, 154, 211
Landolt A. U., 1983, AJ, 88, 439
Landolt A. U., 1992, AJ, 104, 340
Lennarz D., Altmann D., Wiebusch C., 2012, A&A, 538, A120

Li W. D. et al., 2000, in Holt S. S., Zhang W. W., eds, AIP Conf. Proc. Vol. 522, Cosmic Explosions: Tenth Astrophysics Conference. Am. Inst. Phys., New York, p. 103

Lochner M., McEwen J. D., Peiris H. V., Lahav O., Winter M. K., 2016, ApJS, 225, 31

Miller J. S., Stone R. P. S., 1993, Lick Obs. Tech. Rep. 66. Lick Observatory, Santa Cruz, CA

Noebauer U. M., Taubenberger S., Blinnikov S., Sorokina E., Hillebrandt W., 2016, MNRAS, 463, 2972

Nugent P. E. et al., 2011, Nature, 480, 344

Oke J. B., Sandage A., 1968, ApJ, 154, 21

Pan Y.-C. et al., 2015, MNRAS, 452, 4307

Perlmutter S. et al., 1999, ApJ, 517, 565

Phillips M. M., 1993, ApJ, 413, L105

Phillips M. M. et al., 2007, PASP, 119, 360

Prieto J. L., Rest A., Suntzeff N. B., 2006, ApJ, 647, 501

Richmond M. W., Smith H. A., 2012, J. Am. Assoc. Var. Star Obs., 40, 872

Riess A. G., Press W. H., Kirshner R. P., 1996, ApJ, 473, 88

Riess A. G. et al., 1998, AJ, 116, 1009

Riess A. G. et al., 1999, AJ, 117, 707

Riess A. G. et al., 2016, ApJ, 826, 56

Riess A. G., Casertano S., Yuan W., Macri L. M., Scolnic D., 2019, ApJ, 876, 85

Scalzo R. A. et al., 2010, ApJ, 713, 1073

Schlafly E. F., Finkbeiner D. P., 2011, ApJ, 737, 103

Schlegel D. J., Finkbeiner D. P., Davis M., 1998, ApJ, 500, 525

Shivvers I. et al., 2016, MNRAS, 461, 3057

Silverman J. M., Ganeshalingam M., Li W., Filippenko A. V., Miller A. A., Poznanski D., 2011, MNRAS, 410, 585

Silverman J. M. et al., 2012a, ApJ, 756, L7

Silverman J. M. et al., 2012b, MNRAS, 425, 1789

Silverman J. M., Ganeshalingam M., Filippenko A. V., 2013, MNRAS, 430, 1030

Stritzinger M. et al., 2002, AJ, 124, 2100

Stritzinger M. D. et al., 2011, AJ, 142, 156

Tonry J. L. et al., 2012, ApJ, 750, 99

Vinkó J. et al., 2012, A&A, 546, A12

Zhang K. et al., 2016, ApJ, 820, 67

Zheng W. et al., 2013, ApJ, 778, L15

Zheng W. et al., 2014, ApJ, 783, L24

Zheng W., et al., 2017, ApJ, 841, 64

Zheng W., Kelly P. L., Filippenko A. V., 2018, ApJ, 858, 104

SUPPORTING INFORMATION

Supplementary data are available at *MNRAS* online.

Table 2. Photometry of 93 SNe Ia.
Table B3. Natural-system photometry of 93 SNe Ia.

Please note: Oxford University Press is not responsible for the content or functionality of any supporting materials supplied by the authors. Any queries (other than missing material) should be directed to the corresponding author for the article.

APPENDIX A: SAMPLE INFORMATION

Table A1. SN Ia sample.

SN	R.A.[a] α(2000)	Dec.[a] δ(2000)	Discovery[a] date (UT)	Discovery reference	Spectroscopic[b] reference	Type[c]	Host[a] galaxy	z_{helio}[d]	$E(B-V)_{MW}$[e] (mag)	E[f] (arcsec)	N[f] (arcsec)	Host subtraction[g]
2005hk	6.96196	−1.19792	2005 Oct 30	IAUC 8625	CBET 269, Ph07	Iax	UGC 272	0.013	0.020	16.9	7.5	Y
2005ki	160.11758	9.20233	2005 Nov 18	CBET 294	CBET 296	Ia	NGC 3332	0.019	0.027	−2.2	71.2	N
2006ev	322.74692	13.98922	2006 Sep 12	IAUC 8747	CBET 622	Ia	UGC 11758	0.029	0.077	23.9	11.3	Y
2006mq	121.55162	−27.56261	2006 Oct 22	CBET 721	CBET 724	Ia	ESO 494−G26	0.003	0.362	17.3	−123.1	N
2007F	195.81283	50.61881	2007 Jan 11	CBET 803	CBET 805	Ia	UGC 8162	0.024	0.015	−9.8	−7.0	Y
2007bd	127.88867	−1.19944	2007 Apr 4	CBET 914	CBET 915	Ia	UGC 4455	0.031	0.029	6.0	−6.2	Y
2007bm	171.25958	−9.79828	2007 Apr 20	CBET 936	CBET 939	Ia	NGC 3672	0.006	0.035	−2.5	−10.4	Y
2007fb	359.21821	5.50883	2007 Jul 3	CBET 992	CBET 993	Ia	UGC 12859	0.018	0.048	12.2	1.5	Y
2007fs	330.4185	−21.50822	2007 Jul 15	CBET 1002	CBET 1003	Ia	ESO 601−G5	0.017	0.029	34.5	10.6	Y
2007if	17.71404	15.46108	2007 Aug 16	CBET 1059	CBET 1059	SC	Anon.	0.074±	0.071	–	–	N
2007jg	52.46175	0.05683	2007 Sep 14	CBET 1076	CBET 1076	Ia	SDSS J032950.83+000316.0†	0.037	0.091	−0.1	8.6	Y
2007kk	55.59692	39.24178	2007 Sep 28	CBET 1096	CBET 1097	Ia	UGC 2828	0.041	0.196	−9.1	−9.9	Y
2008Y	169.87737	54.46283	2008 Feb 6	CBET 1240	CBET 1246	Ia	MCG +09−19−39	0.070	0.011	−2.3	7.1	Y
2008dh	8.79717	23.25419	2008 Jun 8	CBET 1409	CBET 1409	Ia	PGC 1684149†	0.037	0.026	12.2	−3.0	Y
2008ds	7.46179	31.39275	2008 Jun 28	CBET 1419	CBET 1419	Ia-pec	UGC 299	0.021	0.055	−33.0	−2.2	Y
2008eg	27.90112	19.10469	2008 Jul 20	CBET 1444	CBET 1444	Ia	UGC 1324	0.034	0.057	0.3	4.3	Y
2008ek	241.38821	17.59256	2008 Jul 28	CBET 1452	CBET 1454	Ia	IC 1181	0.033	0.038	−9.7	−4.1	Y
2008eo	10.46683	32.99033	2008 Aug 3	CBET 1459	CBET 1465	Ia	UGC 442	0.016	0.070	4.4	−3.5	Y
2008eq	255.03	23.13239	2008 Aug 2	CBET 1460	CBET 1465	Ia	PGC 214560†	0.057	0.063	4.1	3.6	Y
2008fk	38.52108	1.39514	2008 Sep 2	CBET 1494	CBET 1499	Ia	2MASX J02340513+0123408†	0.072	0.020	−1.2	1.9	N
2008fu	45.61875	−24.45597	2008 Sep 25	CBET 1517	CBET 1519	Ia	ESO 480−IG21	0.052	0.019	−2.6	−0.5	Y
2008gg	21.346	−18.17244	2008 Oct 9	CBET 1538	CBET 1540	Ia	NGC 539	0.032	0.021	18.7	−30.9	N
2008gl	20.22842	4.80531	2008 Oct 20	CBET 1545	CBET 1547	Ia	UGC 881	0.034	0.024	20.2	14.3	Y
2008go	332.68679	−20.78811	2008 Oct 22	CBET 1553	CBET 1554	Ia	Anon.†	0.062	0.032	11.9	8.8	N
2008gp	50.75304	1.36189	2008 Oct 27	CBET 1555	CBET 1558	Ia	MCG +00−9−74	0.033	0.104	10.9	−14.0	Y
2008ha	353.71954	18.2265	2008 Nov 7	CBET 1567	CBET 1576	Iax	UGC 12682	0.005	0.068	−11.5	−2.6	Y
2008hs	36.37342	41.84308	2008 Dec 1	CBET 1598	CBET 1599	Ia	NGC 910	0.017	0.049	31.7	67.7	N
2009D	58.59512	−19.18172	2009 Jan 2	CBET 1647	CBET 1647	Ia	MCG −03−10−52	0.025	0.046	−26.1	30.9	N
2009al	162.84196	8.57853	2009 Feb 26	CBET 1705	CBET 1708	Ia	NGC 3425†	0.022	0.021	−51.3	41.0	N
2009an	185.69779	65.85117	2009 Feb 27	CBET 1707	CBET 1709	Ia	NGC 4332	0.009	0.016	4.4	26.6	Y
2009dc	237.8005	25.70778	2009 Apr 9	CBET 1762	CBET 1776	SC	UGC 10064	0.021	0.060	−15.7	21.1	Y
2009ee	170.35542	34.33981	2009 May 9	CBET 1795	CBET 1802	Ia	IC 2738	0.035	0.021	27.7	−60.7	N
2009eq	280.03458	40.12681	2009 May 11	CBET 1805	CBET 1817	Ia-pec	NGC 6686	0.024	0.053	14.7	−39.0	N
2009eu	247.17137	39.55347	2009 May 21	CBET 1813	CBET 1817	Ia	NGC 6166	0.030	0.010	30.6	6.9	Y
2009fv	247.43425	40.81161	2009 Jun 2	CBET 1834	CBET 1846	Ia	NGC 6173	0.029	0.005	−7.7	0.0	Y
2009hn	38.00129	1.24819	2009 Jul 24	CBET 1886	CBET 1889	Ia	UGC 2005	0.022	0.021	38.1	6.0	Y
2009hp	44.59983	6.59308	2009 Jul 26	CBET 1888	CBET 1889	Ia	MCG +01−08−30	0.021	0.198	−9.2	4.6	Y
2009hs	268.96221	62.59975	2009 Jul 28	CBET 1892	CBET 1909	91bg-like	NGC 6521	0.027	0.035	17.2	−45.0	Y
2009ig	39.54837	−1.31253	2009 Aug 20	CBET 1918	CBET 1918	Ia	NGC 1015	0.009	0.028	0.7	22.2	Y
2009kq	129.06288	28.06714	2009 Nov 5	CBET 2005	ATEL 2291	Ia	MCG +05−21−1	0.012	0.035	−4.2	24.5	Y
2010ao	205.92079	3.90003	2010 Mar 18	CBET 2211	CBET 2223	Ia	UGC 8686	0.023	0.023	11.8	14.5	Y
2010hs	36.41308	24.76489	2010 Sep 12	CBET 2454	CBET 2461	Ia	PGC 1715790†	0.076∓	0.100	−93.4	−46.4	N
2010ii	339.55492	35.49167	2010 Sep 30	CBET 2474	CBET 2474	Ia	NGC 7342	0.027	0.075	0.4	−25.9	Y
2010ju	85.48329	18.4975	2010 Nov 14	CBET 2549	CBET 2550	Ia	UGC 3341	0.015	0.361	6.3	18.5	Y
2011M	75.17312	62.24406	2011 Jan 19	CBET 2640	CBET 2640	Ia	UGC 3218	0.017	0.352	−15.1	0.1	Y

Table A1 – continued

SN	R.A.[a] α (2000)	Dec.[a] δ (2000)	Discovery[a] date (UT)	Discovery reference	Spectroscopic[b] reference	Type[c]	Host[a] galaxy	$z_{\rm helio}$[d]	$E(B-V)_{\rm MW}$[e] (mag)	E[f] (arcsec)	N[f] (arcsec)	Host subtraction[g]
2011bd	266.77633	57.30131	2011 Mar 24	CBET 2685	CBET 2685	Ia	NGC 6473	0.028‡	0.041	3.3	−31.0	Y
2011by	178.93983	55.32606	2011 Apr 26	CBET 2708	CBET 2708	Ia	NGC 3972	0.003	0.012	4.0	19.1	Y
2011df	291.89017	54.38647	2011 May 21	CBET 2729	CBET 2729	Ia	NGC 6801	0.014	0.112	−19.0	48.9	Y
2011dl	244.52071	21.55111	2011 Jun 17	CBET 2744	CBET 2744	Ia	UGC 10321	0.026‡	0.067	−18.6	−35.0	N
2011dz	243.18675	28.28422	2011 Jun 26	CBET 2761	CBET 2761	Ia	UGC 10273	0.025	0.044	−2.4	−61.8	Y
2011ek	36.45371	18.53333	2011 Aug 4	CBET 2783	CBET 2783	Ia	NGC 918	0.005	0.307	−27.7	133.5	Y
2011fe	210.77421	54.27372	2011 Aug 24	CBET 2792	CBET 2792	Ia	M101‡	0.001	0.008	−59.3	−270.1	Y
2011fs	334.33133	35.58056	2011 Sep 15	CBET 2825	CBET 2825	Ia	UGC 11975	0.021	0.101	−2.7	33.8	N
2012E	38.34496	9.58489	2012 Jan 14	CBET 2981	CBET 2981	Ia	NGC 975	0.020	0.063	0.6	−60.5	N
2012Z	50.52229	−15.38767	2012 Jan 29	CBET 3014	CBET 3014	Iax	NGC 1309	0.007	0.034	−17.5	44.6	N
2012bh	183.40546	46.48347	2012 Mar 11	CBET 3066	CBET 3066	Ia	UGC 7228	0.025	0.016	5.2	−37.8	N
2012cg	186.80346	9.42033	2012 May 17	CBET 3111	CBET 3111	Ia	NGC 4424	0.001	0.018	18.1	−1.2	Y
2012dn	305.90108	−28.27872	2012 Jul 8	CBET 3174	CBET 3174	SC	PGC 64605‡	0.010	0.052	–	–	Y
2012ea	266.29333	18.14078	2012 Aug 8	CBET 3199	CBET 3199	91bg-like	NGC 6430	0.010	0.055	−55.2	6.6	N
2012gl	153.20967	12.68242	2012 Oct 29	CBET 3302	CBET 3302	Ia	NGC 3153	0.009	0.036	−2.6	56.7	N
2013bs	259.34179	41.06672	2013 Apr 18	CBET 3494	CBET 3494	Ia	NGC 6343	0.028	0.025	65.1	50.4	N
2013dh	232.50454	12.98692	2013 Jun 12	CBET 3561	CBET 3561	91T-like	NGC 5936	0.013	0.033	3.8	−8.7	Y
2013dr	259.87608	47.70128	2013 Jul 1	CBET 3576	CBET 3576	Ia	PGC 60077‡	0.017	0.021	−8.7	−4.3	Y
2013dy	334.57333	40.56933	2013 Jul 10	CBET 3588	CBET 3588	Ia	NGC 7250	0.004	0.132	−2.3	25.0	Y
2013ex	83.19425	−14.04594	2013 Aug 19	CBET 3635	CBET 3635	Ia	NGC 1954	0.010	0.123	−24.9	60.6	N
2013fa	310.97321	12.51436	2013 Aug 25	CBET 3641	CBET 3641	Ia	NGC 6956	0.016	0.086	−2.1	8.8	Y
2013fw	318.43654	13.57592	2013 Oct 21	CBET 3681	CBET 3681	Ia	NGC 7042	0.017	0.067	−15.9	3.6	Y
2013gh	330.591	−18.91678	2013 Aug 8	CBET 3706	CBET 3706	Ia	NGC 7183	0.009	0.025	3.1	−1.0	Y
2013gq	124.47275	23.46958	2013 Mar 25	CBET 3730	CBET 3730	Ia	NGC 2554	0.014	0.049	−0.4	−9.2	Y
2013gy	55.57033	−4.72181	2013 Dec 6	CBET 3743	CBET 3743	Ia	NGC 1418	0.014	0.050	10.8	32.2	N
2014J	148.92558	69.67389	2014 Jan 21	CBET 3792	CBET 3792	Ia	NGC 3034	0.001	0.136	−55.2	−19.8	N
2014ai	139.93404	33.76378	2014 Mar 21	CBET 3838	CBET 3838	Ia	NGC 2832	0.023	0.015	−33.5	50.5	Y
2014ao	128.63883	−2.54336	2014 Apr 17	CBET 3855	CBET 3855	Ia	NGC 2615	0.014	0.031	−0.4	12.4	Y
2014bj	290.66312	43.89081	2014 Oct 29	CBET 3893	CBET 3893	Ia	Anon.	0.005‡	0.091	–	–	N
2014dt	185.48987	4.47181	2014 Oct 29	CBET 4011	CBET 4011	Iax	NGC 4303	0.005	0.019	39.9	−6.6	Y
2015N	325.82037	43.57989	2015 Jul 6	CBET 4124	CBET 4124	Ia	UGC 11797	0.019	0.456	−36.1	12.9	Y
2016aew	212.86037	1.28596	2016 Feb 12	TNSTR–2016–106	TNSCR–2016–114	Ia	IC 0986	0.025	0.033	3.9	−2.0	Y
2016coj	182.02833	65.17729	2016 May 28	TNSTR–2016–384	TNSCR–2016–386	Ia	NGC 4125	0.005	0.016	4.9	11.3	Y
2016fbk	26.02737	34.38283	2016 Aug 16	TNSTR–2016–568	TNSCR–2016–572	Ia	UGC 01212	0.036	0.042	−19.6	−16.1	Y
2016ffh	227.95617	46.25089	2016 Aug 17	TNSTR–2016–583	TNSCR–2016–589	Ia	CGCG 249–011	0.018	0.024	11.4	−10.7	Y
2016gcl	354.48592	27.27715	2016 Sep 8	TNSTR–2016–644	TNSCR–2016–655	91T-like	AGC 331536	0.028	0.063	−2.7	−1.5	Y
2016gdt	328.09396	3.42181	2016 Sep 8	TNSTR–2016–652	TNSCR–2016–666	91bg-like	IC 1407	0.029	0.072	−13.3	−19.3	N
2016hvl	101.009	12.39662	2016 Nov 4	TNSTR–2016–884	TNSCR–2016–892	Ia	UGC 3524	0.013	0.377	22.9	−19.2	N
2017cfd	130.20479	73.48754	2017 Mar 16	TNSTR–2017–315	TNSCR–2017–325	Ia	IC 511	0.012	0.019	−5.5	3.1	Y
2017drh	263.10854	7.0632	2017 May 3	TNSTR–2017–513	TNSCR–2017–516	Ia	NGC 6384	0.006	0.106	26.1	10.5	Y
2017dws	235.05904	11.34486	2017 May 3	TNSTR–2017–528	TNSCR–2017–534	Ia	Anon.	0.082‡	0.035	–	–	Y
2017erp	227.31171	−11.33422	2017 Jun 13	TNSTR–2017–647	TNSCR–2017–655	Ia	NGC 5861	0.006	0.093	−18.8	−45.2	N
2017fgc	20.06017	3.40277	2017 Jul 11	TNSTR–2017–753	TNSCR–2017–757	Ia	NGC 0474	0.008	0.029	116.0	−45.4	N
2017glx	295.91787	56.11008	2017 Sep 3	TNSTR–2017–963	TNSCR–2017–970	91T-like	NGC 6824	0.011	0.107	−3.4	2.2	Y
2017hbi	38.13154	35.4836	2017 Oct 2	TNSTR–2017–1066	TNSCR–2017–1074	Ia	Anon.	0.040‡	0.061	–	–	N
2018aoz	177.75762	−28.74406	2018 Apr 2	TNSTR–2018–428	TNSCR–2018–433	Ia	NGC 3923	0.006	0.072	1.8	223.1	N

Table A1 – *continued*

SN	R.A.[a] α (2000)	Dec.[a] δ (2000)	Discovery[a] date (UT)	Discovery reference	Spectroscopic[b] reference	Type[c]	Host[a] galaxy	z_{helio}[d]	$E(B-V)_{\text{MW}}$[e] (mag)	E'[f] (arcsec)	N'[f] (arcsec)	Host subtraction[g]
2018dem	317.99387	−0.2181	2018 Jul 8	TNSTR–2018–947	TNSCR–2018–1219	Ia	SDSS J211158.77−001309.9	0.060	0.072	−3.6	4.8	Y
2018gv	121.39421	−11.43786	2018 Jan 15	TNSTR–2018–57	TNSCR–2018–75	Ia	NGC 2525	0.005	0.050	−50.4	−39.0	Y

Notes. [a]Basic information for each SN, including its J2000 right ascension and declination (in decimal degrees), its host galaxy, and its discovery date, were sourced from TNS. However, host galaxies marked with a '†' symbol were obtained from Lennarz, Altmann & Wiebusch (2012), while those with a '‡' are from the given discovery reference.
[b]Spectroscopic classification reference. Ph07 refers to Phillips et al. (2007).
[c]Spectroscopic type as classified in the spectroscopic reference. Super-Chandrasekhar candidates are labelled with 'SC'.
[d]Host-galaxy heliocentric redshifts are from NED unless otherwise indicated. Those marked with a '†' symbol were obtained from their spectroscopic references, and '±' refers to Scalzo et al. (2010) and '∓' to Lennarz et al. (2012).
[e]Extinction is calculated at the SN position using the dust maps of Schlegel, Finkbeiner & Davis (1998) subject to the recalibration of Schlafly & Finkbeiner (2011).
[f]Offsets from host-galaxy nuclei are computed using the host location as given by NED (if available) for all SNe except SN 2010hs, whose host coordinates are from the catalogue of Lennarz et al. (2012).
[g]Indicates whether the SN had its host galaxy subtracted (Y) or not (N).

APPENDIX B: LIGHT CURVES

B1 Light-curve properties

B2 Natural-system light curves

SN light curves have long been released on the Landolt system (e.g. CfA1, CfA2, G10), thus allowing for easy comparison between data sets from different telescopes. Indeed, we analysed our light curves only after transforming to the Landolt system – a decision motivated largely by the fact that our data set is derived from observations collected with four distinct telescope/CCD/filter combinations. However, there are instances where natural-system light curves are more attractive. Since the stellar SEDs that are used to derive colour terms do not accurately reflect those of SNe Ia, SN photometry transformed using such colour terms will not necessarily be on the Landolt system. Conventionally, second-order 'S-corrections' are performed to properly account for the SN SED by using a selected spectral series (Stritzinger et al. 2002), but many groups are now releasing their low-z SN Ia photometry data sets in the natural systems of their telescopes along with the transmission curves of their photometry systems (e.g. CfA3, CfA4, CSP1-3). Thus, given a spectral series (e.g. Hsiao et al. 2007) and transmission functions, one can transform photometry from one system to another without the need for colour corrections. In turn, this should provide less scatter in SN flux measurements.

The aforementioned benefits motivate us to release our photometric data set (see Section 4) in the relevant natural systems in addition to the Landolt system. A table of natural-system magnitudes analogous to Table 2 is available for our entire data set, with a sample given in Table B3. We reiterate that owing to changes in the observing equipment, there are four transmission curves (KAIT3, KAIT4, Nickel1, Nickel2) for each bandpass. Any analysis of the data set as a whole should therefore be done either on the Landolt system or after transforming all of the data to a common system (see appendix A of Ganeshalingam, Li & Filippenko 2013). Transmission curves for all filter and system combinations covered by our data set are archived with the journal and available online in our SNDB.
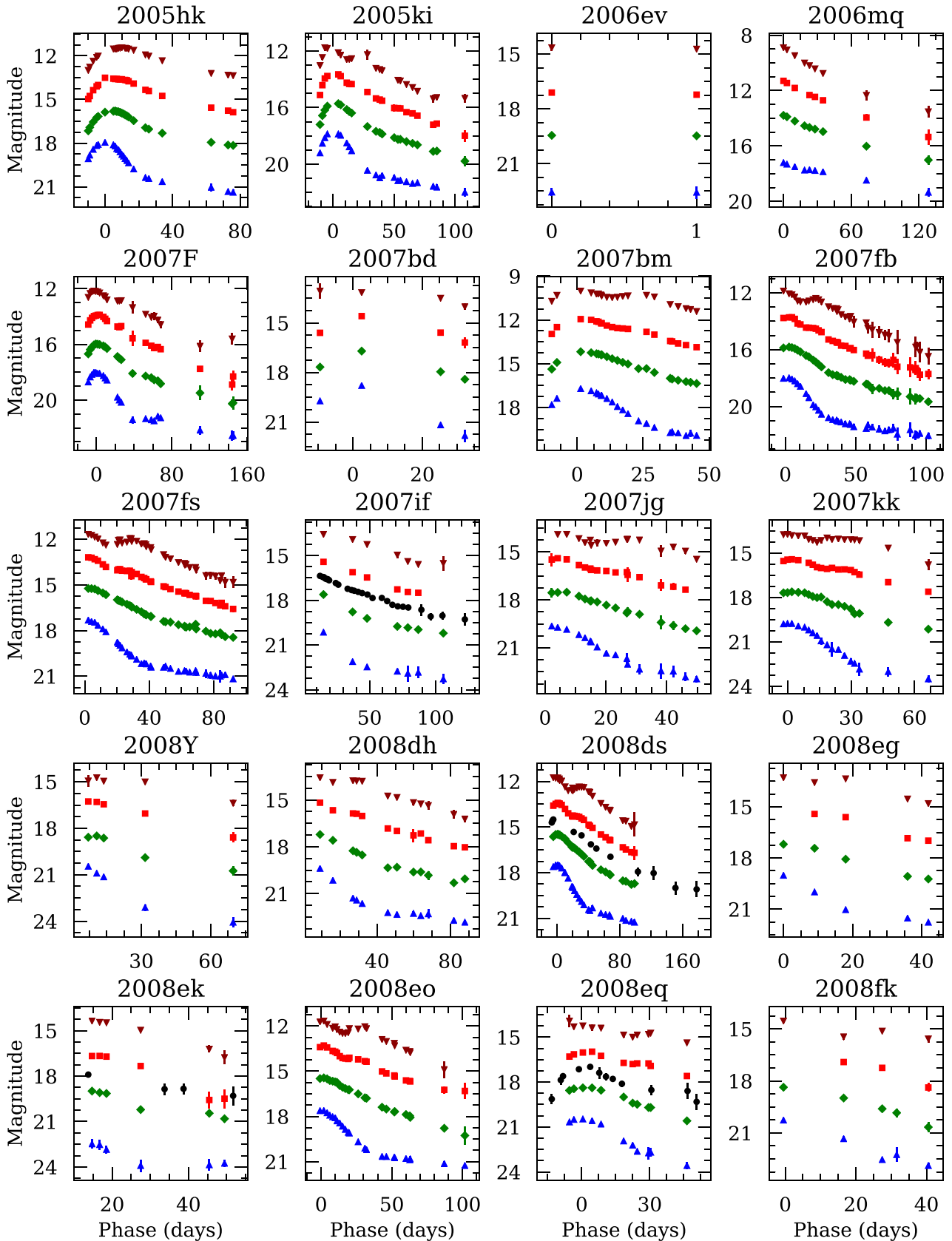
Figure B1. Observed *BVRI* and unfiltered light curves of our SN Ia sample. Blue up-triangles are *B* + 2, green diamonds are *V*, red squares are *R* − 2, dark red down-triangles are *I* − 4, and black circles are Clear − 1. In most cases, the error bars are smaller than the points themselves. All dates have been shifted relative to the time of maximum *B*-band brightness, if determined, and relative to the time of the first epoch otherwise.
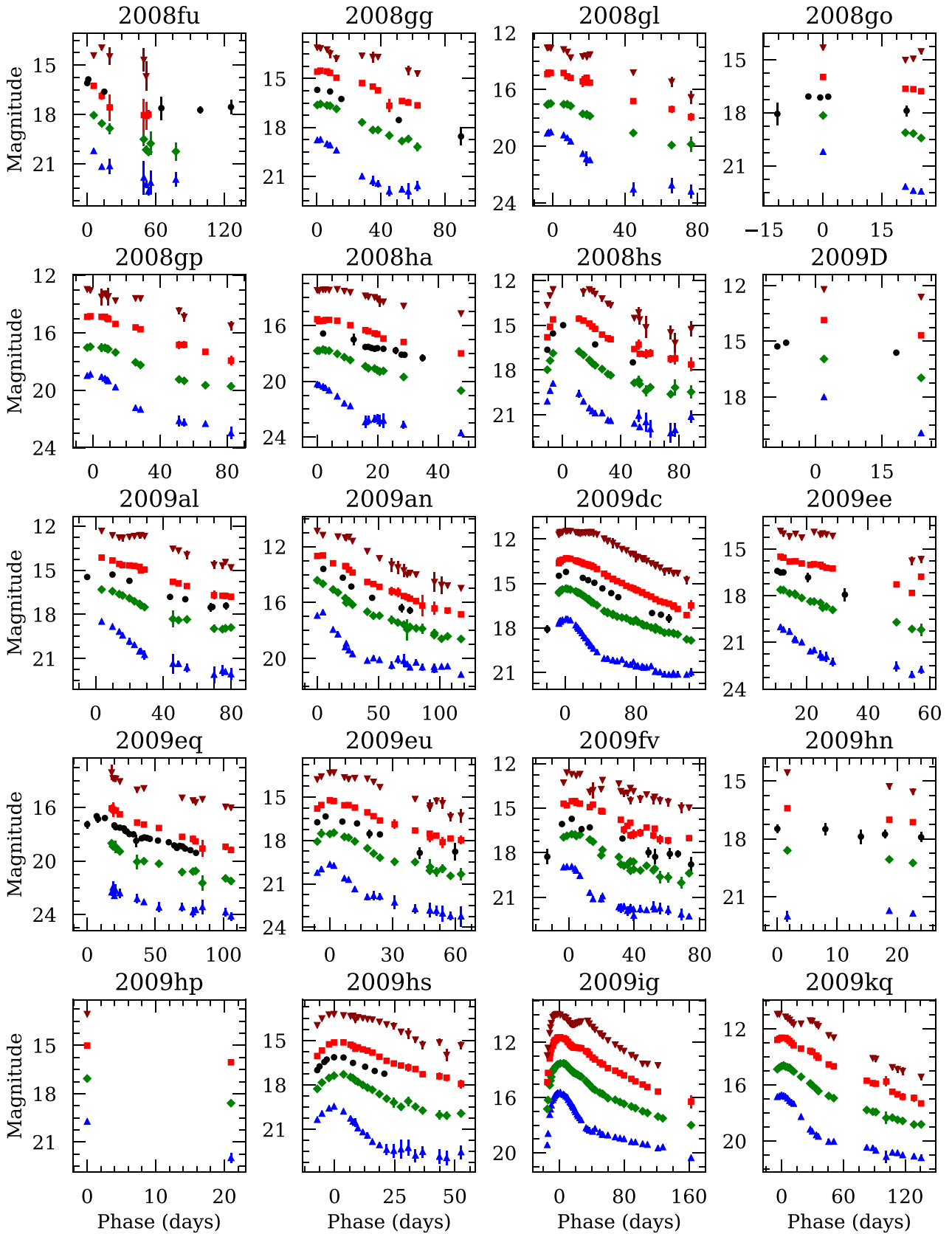
Figure B1– *continued*
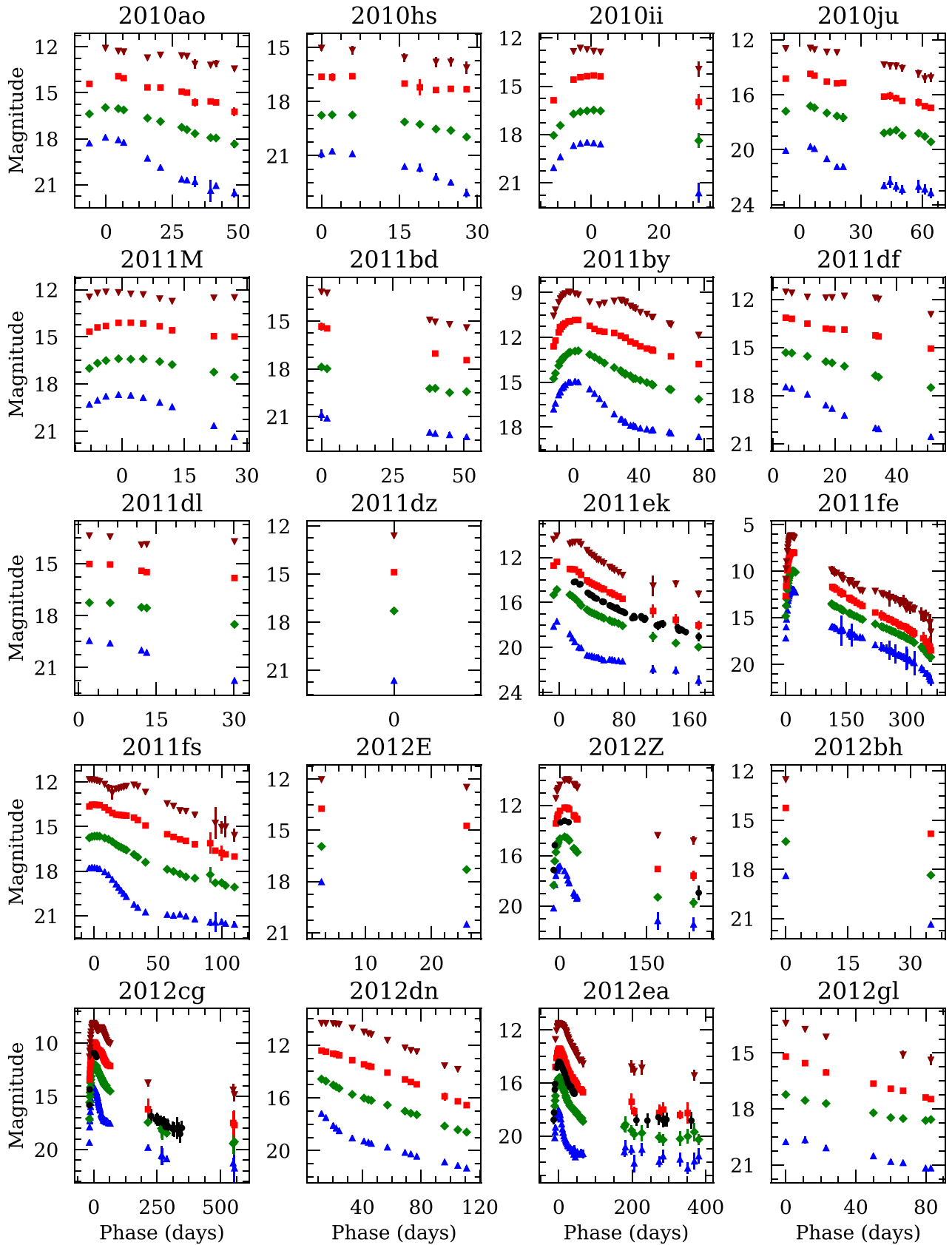
Figure B1– *continued*
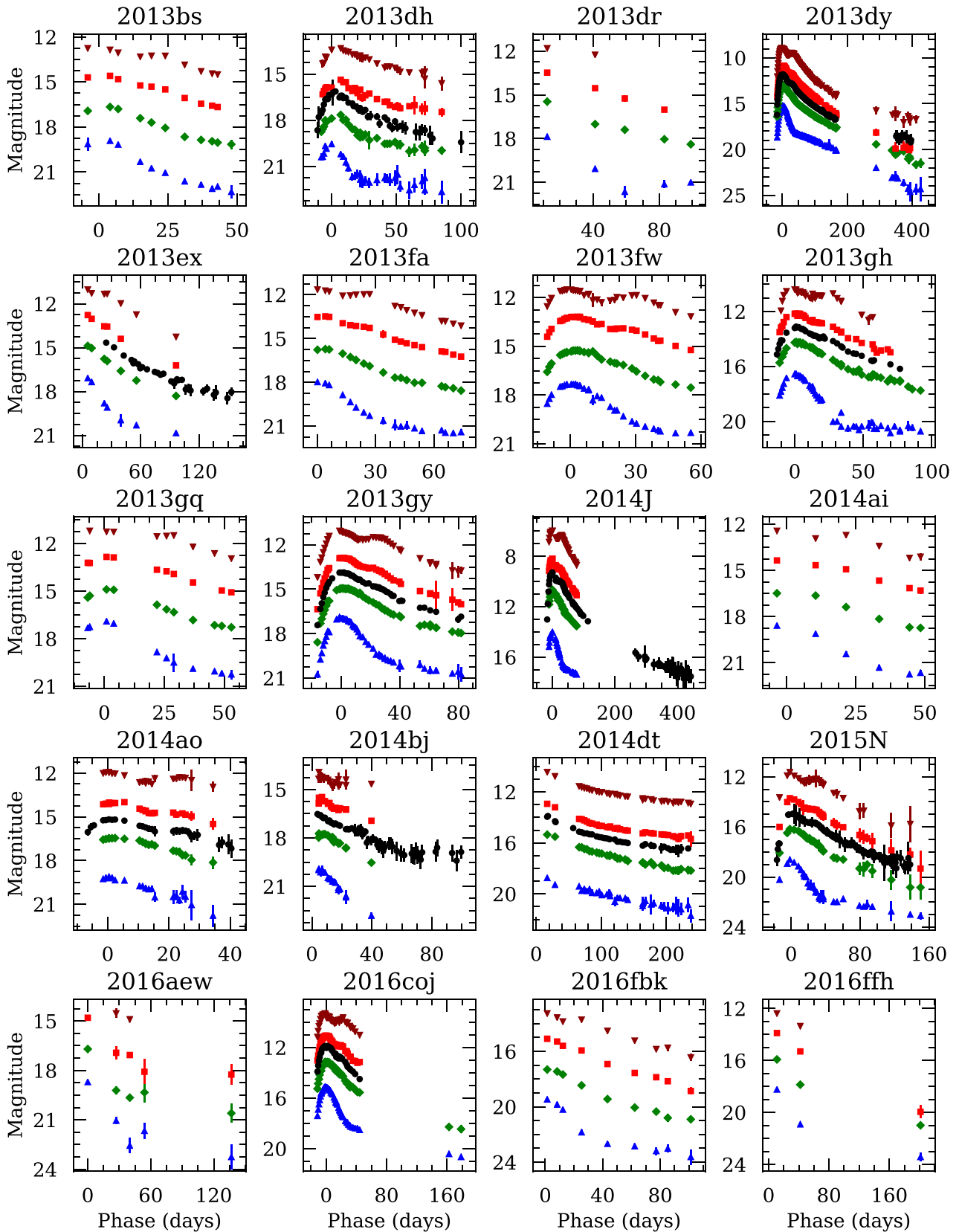
Figure B1– *continued*
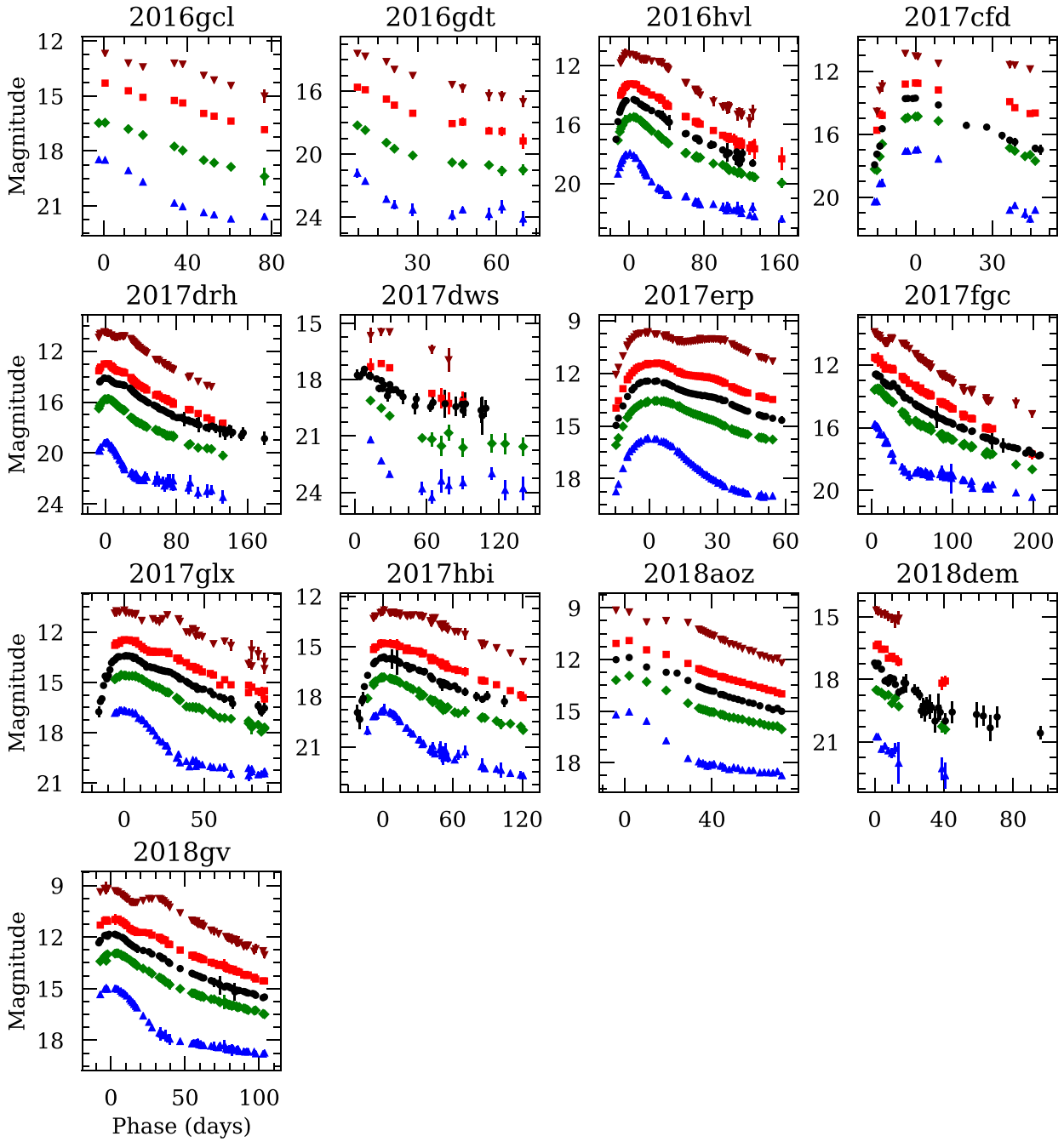
Figure B1– *continued*

Table B1. Light-curve properties derived from Gaussian process interpolation.

SN	$t_{B_{max}}$ (MJD)	B_{max} (mag)	$\Delta m_{15}(B)$ (mag)	$t_{V_{max}}$ (MJD)	V_{max} (mag)	$\Delta m_{15}(V)$ (mag)	$(B-V)_{B_{max}}$ (mag)
2005hk	53684.32 ± 0.29	15.850 ± 0.022	1.580 ± 0.053	53688.11 ± 0.56	15.703 ± 0.018	0.799 ± 0.039	0.069 ± 0.029
2005ki	53704.67 ± 0.40	15.572 ± 0.042	1.275 ± 0.080	53705.97 ± 0.56	15.534 ± 0.043	0.826 ± 0.067	0.021 ± 0.060
2007F	54122.32 ± 0.45	15.975 ± 0.016	0.864 ± 0.085	54124.03 ± 0.54	15.928 ± 0.011	0.550 ± 0.069	0.029 ± 0.020
2007bd	54210.22 ± 1.87	16.680 ± 0.051	1.451 ± 0.248	54212.58 ± 1.74	16.552 ± 0.074	0.891 ± 0.177	0.095 ± 0.090
2007bm	54224.46 ± 0.50	14.548 ± 0.022	1.232 ± 0.057	54225.66 ± 0.39	14.057 ± 0.011	0.690 ± 0.025	0.481 ± 0.025
2007fb	54287.92 ± 0.62	15.792 ± 0.021	1.332 ± 0.093	54288.90 ± 0.65	15.668 ± 0.024	0.726 ± 0.049	0.119 ± 0.032
2007kk	54382.76 ± 1.41	16.953 ± 0.024	0.954 ± 0.169	54385.52 ± 0.98	16.993 ± 0.017	0.559 ± 0.063	− 0.064 ± 0.030
2008ds	54651.90 ± 0.24	15.263 ± 0.009	0.957 ± 0.030	54652.49 ± 0.25	15.303 ± 0.004	0.617 ± 0.019	− 0.042 ± 0.010
2008eo	54688.14 ± 0.81	15.311 ± 0.020	1.026 ± 0.070	54689.74 ± 0.30	15.220 ± 0.006	0.675 ± 0.016	0.074 ± 0.021
2008eq	54689.54 ± 0.93	18.222 ± 0.027	1.029 ± 0.148	54691.77 ± 1.22	18.141 ± 0.029	0.576 ± 0.092	0.064 ± 0.040
2008gg	54749.80 ± 1.50	16.677 ± 0.033	0.983 ± 0.181	54752.39 ± 1.20	16.523 ± 0.029	0.570 ± 0.130	0.130 ± 0.044
2008gl	54767.98 ± 0.83	16.882 ± 0.043	1.394 ± 0.158	54769.51 ± 1.32	16.870 ± 0.039	0.704 ± 0.101	0.005 ± 0.058
2008gp	54779.28 ± 0.85	16.484 ± 0.037	1.136 ± 0.135	54780.97 ± 1.16	16.610 ± 0.038	0.631 ± 0.108	− 0.136 ± 0.053
2008hs	54812.80 ± 0.52	15.932 ± 0.106	1.991 ± 0.160	54814.38 ± 0.54	15.769 ± 0.123	1.228 ± 0.161	0.129 ± 0.162
2009dc	54946.34 ± 0.80	15.148 ± 0.014	0.713 ± 0.060	54946.85 ± 0.85	15.166 ± 0.015	0.294 ± 0.035	− 0.020 ± 0.021
2009eu	54984.59 ± 0.50	17.690 ± 0.054	1.816 ± 0.132	54986.86 ± 0.68	17.464 ± 0.041	1.006 ± 0.091	0.179 ± 0.068
2009fv	54994.47 ± 0.40	16.887 ± 0.024	1.670 ± 0.090	54998.15 ± 1.33	16.775 ± 0.022	0.767 ± 0.123	0.069 ± 0.032
2009hs	55048.55 ± 0.34	17.376 ± 0.041	2.090 ± 0.109	55051.00 ± 0.32	17.170 ± 0.030	1.186 ± 0.058	0.136 ± 0.051
2009ig	55079.70 ± 1.11	13.560 ± 0.032	0.850 ± 0.124	55082.78 ± 0.44	13.427 ± 0.013	0.682 ± 0.023	0.095 ± 0.034
2009kq	55155.05 ± 0.39	14.591 ± 0.014	1.091 ± 0.067	55156.49 ± 0.24	14.540 ± 0.010	0.658 ± 0.023	0.037 ± 0.017
2010ao	55289.32 ± 0.57	15.857 ± 0.037	1.329 ± 0.094	55290.55 ± 0.59	15.921 ± 0.024	0.693 ± 0.053	− 0.073 ± 0.045
2010ii	55480.46 ± 0.21	16.207 ± 0.011	1.034 ± 0.317	55481.61 ± 0.47	16.248 ± 0.012	0.769 ± 0.241	− 0.052 ± 0.016
2010ju	55525.65 ± 1.04	16.136 ± 0.073	1.315 ± 0.106	55526.39 ± 1.01	15.628 ± 0.056	0.715 ± 0.053	0.505 ± 0.092
2011M	55593.45 ± 0.26	15.225 ± 0.014	1.136 ± 0.050	55595.27 ± 0.32	15.228 ± 0.013	0.649 ± 0.050	− 0.023 ± 0.019
2011by	55690.56 ± 0.68	12.906 ± 0.018	1.085 ± 0.095	55692.59 ± 0.62	12.874 ± 0.015	0.695 ± 0.052	0.014 ± 0.024
2011ek	55789.58 ± 0.85	14.504 ± 0.123	1.272 ± 0.190	55790.80 ± 0.67	13.715 ± 0.061	0.795 ± 0.092	0.775 ± 0.137
2011fs	55832.32 ± 0.69	15.357 ± 0.009	0.808 ± 0.071	55835.04 ± 0.57	15.313 ± 0.008	0.565 ± 0.035	0.018 ± 0.012
2012Z	55965.90 ± 0.38	14.662 ± 0.026	1.199 ± 0.074	55973.93 ± 0.86	14.377 ± 0.016	0.790 ± 0.066	0.105 ± 0.030
2012cg	56081.36 ± 0.26	12.115 ± 0.012	0.906 ± 0.032	56083.25 ± 0.24	11.952 ± 0.005	0.631 ± 0.013	0.144 ± 0.013
2012ea	56157.89 ± 0.11	15.848 ± 0.009	1.945 ± 0.028	56160.18 ± 0.14	15.403 ± 0.007	1.224 ± 0.018	0.387 ± 0.012
2013bs	56406.88 ± 1.68	16.697 ± 0.090	1.533 ± 0.144	56409.11 ± 0.71	16.589 ± 0.038	0.903 ± 0.049	0.073 ± 0.098
2013dh	56463.02 ± 0.62	17.507 ± 0.069	1.554 ± 0.155	56467.07 ± 0.54	17.524 ± 0.048	1.014 ± 0.071	− 0.151 ± 0.084
2013dy	56500.40 ± 0.19	12.697 ± 0.008	0.870 ± 0.023	56501.84 ± 0.34	12.578 ± 0.005	0.609 ± 0.021	0.109 ± 0.010
2013fw	56601.14 ± 0.26	15.078 ± 0.006	1.038 ± 0.037	56603.53 ± 0.29	15.059 ± 0.006	0.630 ± 0.021	− 0.010 ± 0.008
2013gh	56527.13 ± 0.41	14.434 ± 0.028	1.223 ± 0.050	56529.24 ± 0.49	14.180 ± 0.011	0.606 ± 0.029	0.225 ± 0.030
2013gq	56384.64 ± 0.66	14.738 ± 0.029	1.229 ± 0.154	56386.45 ± 0.77	14.753 ± 0.019	0.645 ± 0.072	− 0.035 ± 0.035
2013gy	56647.80 ± 0.65	14.751 ± 0.025	1.247 ± 0.072	56650.05 ± 0.55	14.803 ± 0.006	0.644 ± 0.034	− 0.071 ± 0.025
2014J	56688.93 ± 0.65	11.452 ± 0.020	0.890 ± 0.074	56689.71 ± 0.50	10.237 ± 0.017	0.553 ± 0.033	1.211 ± 0.026
2015N	57222.81 ± 0.27	14.853 ± 0.025	1.109 ± 0.078	57225.28 ± 0.79	14.768 ± 0.032	0.628 ± 0.054	0.040 ± 0.041
2016coj	57547.15 ± 0.19	13.082 ± 0.007	1.329 ± 0.030	57547.89 ± 0.18	13.088 ± 0.007	0.681 ± 0.018	− 0.010 ± 0.010
2016gcl	57647.90 ± 1.63	16.227 ± 0.023	0.741 ± 0.126	57650.42 ± 1.18	16.251 ± 0.016	0.543 ± 0.069	− 0.044 ± 0.028
2016hvl	57709.70 ± 0.47	14.392 ± 0.022	1.037 ± 0.055	57713.43 ± 0.67	14.282 ± 0.011	0.619 ± 0.028	0.058 ± 0.025
2017drh	57891.14 ± 0.44	16.691 ± 0.022	1.370 ± 0.065	57891.98 ± 0.48	15.396 ± 0.010	0.720 ± 0.032	1.291 ± 0.024
2017erp	57934.53 ± 0.22	13.336 ± 0.008	1.086 ± 0.031	57937.21 ± 0.35	13.275 ± 0.007	0.667 ± 0.020	0.036 ± 0.010
2017glx	58007.78 ± 0.25	14.228 ± 0.009	0.780 ± 0.026	58009.73 ± 0.87	14.250 ± 0.007	0.493 ± 0.045	− 0.037 ± 0.011
2017hbi	58045.80 ± 0.61	16.580 ± 0.019	0.710 ± 0.074	58045.64 ± 0.76	16.671 ± 0.014	0.310 ± 0.045	− 0.091 ± 0.024
2018aoz	58222.46 ± 0.58	12.761 ± 0.030	1.305 ± 0.124	58223.38 ± 0.46	12.730 ± 0.018	0.779 ± 0.077	0.025 ± 0.035
2018gv	58149.38 ± 0.31	12.751 ± 0.015	0.853 ± 0.037	58153.39 ± 0.32	12.788 ± 0.007	0.740 ± 0.017	− 0.125 ± 0.017

Note. Only those SNe from our sample where the fitting process described in Section 5.1 succeeded appear here.

Table B2. Results of SNOOPY and MLCS2K2 fitting.

SN	SNOOPY $E(B-V)$ fitted parameters				MLCS2K2 fitted parameters			
	t_{max} (MJD)	Δm_{15} (mag)	$E(B-V)_{host}$ (mag)	μ (mag)	t_0 (MJD)	Δ	A_V (mag)	μ (mag)
2005ki	53705.23 ± 0.06	1.419 ± 0.013	-0.011 ± 0.009	34.666 ± 0.013	53705.21 ± 0.11	0.373 ± 0.052	0.027 ± 0.017	34.719 ± 0.065
2007F	54123.83 ± 0.09	1.096 ± 0.012	0.041 ± 0.010	35.163 ± 0.011	54123.13 ± 0.10	-0.179 ± 0.033	0.204 ± 0.036	35.351 ± 0.046
2007bd	54207.12 ± 0.50	1.351 ± 0.067	0.010 ± 0.037	35.748 ± 0.050	54206.65 ± 0.23	0.209 ± 0.103	0.082 ± 0.054	35.851 ± 0.097
2007bm	54225.02 ± 0.15	1.224 ± 0.014	0.588 ± 0.011	32.635 ± 0.019	54223.94 ± 0.08	0.057 ± 0.038	1.109 ± 0.036	32.389 ± 0.048
2007fb	54287.48 ± 0.16	1.353 ± 0.016	0.100 ± 0.009	34.657 ± 0.017	54286.73 ± 0.31	0.285 ± 0.055	0.142 ± 0.042	34.749 ± 0.059
2007fs	54293.70 ± 0.42	0.879 ± 0.015	0.015 ± 0.013	34.505 ± 0.014	54295.17 ± 0.35	-0.161 ± 0.028	0.116 ± 0.032	34.649 ± 0.044
2007if	54338.39 ± 0.86	0.768 ± 0.029	0.034 ± 0.026	36.133 ± 0.033	54343.02 ± 1.17	-0.350 ± 0.062	0.384 ± 0.068	36.245 ± 0.123
2007jg	54365.35 ± 0.47	1.199 ± 0.022	-0.021 ± 0.024	36.493 ± 0.032	54364.35 ± 0.55	-0.025 ± 0.060	0.092 ± 0.051	36.616 ± 0.071
2007kk	54383.83 ± 0.26	1.088 ± 0.035	-0.004 ± 0.022	36.267 ± 0.025	54382.59 ± 0.44	-0.340 ± 0.041	0.168 ± 0.071	36.558 ± 0.066
2008Y	54499.62 ± 1.52	0.939 ± 0.126	0.164 ± 0.045	37.425 ± 0.078	54498.33 ± 1.66	-0.110 ± 0.112	0.226 ± 0.090	37.503 ± 0.127
2008dh	54625.56 ± 0.67	0.924 ± 0.035	0.026 ± 0.024	36.282 ± 0.020	54626.31 ± 0.66	-0.124 ± 0.052	0.077 ± 0.044	36.436 ± 0.077
2008ds	54651.45 ± 0.15	0.865 ± 0.010	-0.013 ± 0.007	34.746 ± 0.011	54652.06 ± 0.18	-0.270 ± 0.023	0.045 ± 0.027	34.975 ± 0.039
2008ek	54668.63 ± 2.52	1.813 ± 0.033	0.669 ± 0.145	36.434 ± 0.096	54662.46 ± 1.63	1.213 ± 0.141	0.220 ± 0.135	35.997 ± 0.120
2008eo	54686.91 ± 0.38	0.884 ± 0.018	0.095 ± 0.015	34.513 ± 0.015	54688.23 ± 0.30	-0.197 ± 0.028	0.261 ± 0.039	34.630 ± 0.045
2008eq	54689.59 ± 0.28	0.971 ± 0.032	0.207 ± 0.015	37.155 ± 0.036	54689.46 ± 0.34	-0.227 ± 0.053	0.444 ± 0.048	37.277 ± 0.068
2008fk	54722.03 ± 1.02	1.263 ± 0.074	-0.197 ± 0.067	37.749 ± 0.091	54719.62 ± 0.99	-0.229 ± 0.084	0.028 ± 0.020	37.967 ± 0.087
2008gg	54750.61 ± 0.58	1.087 ± 0.060	0.111 ± 0.036	35.720 ± 0.050	54749.06 ± 0.72	-0.350 ± 0.046	0.267 ± 0.051	36.047 ± 0.071
2008gl	54766.97 ± 0.27	1.178 ± 0.027	0.124 ± 0.012	35.917 ± 0.024	54767.32 ± 0.37	0.189 ± 0.109	0.227 ± 0.058	35.913 ± 0.086
2008go	54765.09 ± 1.09	1.158 ± 0.101	0.081 ± 0.022	37.167 ± 0.073	54764.78 ± 0.65	0.002 ± 0.118	0.191 ± 0.062	37.317 ± 0.109
2008gp	54779.01 ± 0.08	1.087 ± 0.011	-0.048 ± 0.008	35.909 ± 0.009	54778.92 ± 0.35	-0.106 ± 0.064	0.051 ± 0.035	36.094 ± 0.073
2008hs	54813.07 ± 0.11	1.720 ± 0.012	0.103 ± 0.017	34.836 ± 0.033	54812.83 ± 0.08	1.181 ± 0.042	0.011 ± 0.010	34.297 ± 0.058
2009D	54841.02 ± 0.54	0.932 ± 0.041	0.026 ± 0.017	35.140 ± 0.018	54841.93 ± 1.47	-0.138 ± 0.108	0.125 ± 0.056	35.248 ± 0.080
2009al	54896.75 ± 0.35	1.106 ± 0.029	0.264 ± 0.022	35.127 ± 0.023	54894.38 ± 0.79	-0.264 ± 0.043	0.503 ± 0.054	35.305 ± 0.066
2009dc	–	–	–	–	54945.34 ± 0.16	-0.693 ± 0.017	0.348 ± 0.031	34.687 ± 0.037
2009ee	54951.64 ± 0.80	1.273 ± 0.021	0.210 ± 0.056	36.209 ± 0.042	54949.75 ± 0.71	0.466 ± 0.086	0.085 ± 0.076	36.068 ± 0.085
2009eu	54984.30 ± 0.12	1.787 ± 0.013	0.279 ± 0.021	35.924 ± 0.025	54984.38 ± 0.20	1.199 ± 0.058	0.056 ± 0.046	35.606 ± 0.063
2009hs	55048.76 ± 0.11	1.798 ± 0.013	0.269 ± 0.025	35.728 ± 0.024	55048.51 ± 0.13	1.259 ± 0.034	0.018 ± 0.012	35.404 ± 0.048
2009ig	–	–	–	–	55079.47 ± 0.09	-0.354 ± 0.023	0.123 ± 0.029	33.167 ± 0.039
2009kq	55154.71 ± 0.15	1.103 ± 0.018	0.017 ± 0.011	33.834 ± 0.014	55154.69 ± 0.20	-0.062 ± 0.035	0.154 ± 0.036	33.954 ± 0.047
2010ao	55288.84 ± 0.30	1.129 ± 0.031	0.037 ± 0.019	35.122 ± 0.028	55288.75 ± 0.26	0.009 ± 0.056	0.195 ± 0.048	35.147 ± 0.069
2010ii	–	–	–	–	55481.48 ± 0.19	0.315 ± 0.116	0.031 ± 0.022	35.457 ± 0.096
2010ju	55524.52 ± 0.29	1.175 ± 0.032	0.440 ± 0.023	34.477 ± 0.044	55524.07 ± 0.23	-0.044 ± 0.070	0.931 ± 0.122	34.315 ± 0.107
2011M	55593.49 ± 0.12	1.119 ± 0.025	0.048 ± 0.012	34.482 ± 0.019	55593.14 ± 0.15	-0.008 ± 0.060	0.183 ± 0.107	34.475 ± 0.082
2011by	55690.78 ± 0.09	1.091 ± 0.010	0.094 ± 0.011	32.077 ± 0.011	55690.33 ± 0.09	-0.037 ± 0.029	0.300 ± 0.028	32.071 ± 0.042
2011df	55715.10 ± 0.30	0.943 ± 0.019	0.056 ± 0.010	34.161 ± 0.013	55716.02 ± 0.41	-0.162 ± 0.038	0.215 ± 0.053	34.261 ± 0.056
2011dl	55738.35 ± 0.50	1.089 ± 0.046	0.169 ± 0.033	36.079 ± 0.031	55736.95 ± 0.77	-0.278 ± 0.060	0.439 ± 0.053	36.228 ± 0.064
2011ek	55789.74 ± 0.10	1.522 ± 0.021	0.503 ± 0.012	32.250 ± 0.026	55789.14 ± 0.15	0.562 ± 0.073	0.979 ± 0.101	31.821 ± 0.090
2011fe	55815.22 ± 0.06	1.096 ± 0.005	-0.006 ± 0.005	29.228 ± 0.006	–	–	–	–
2011fs	55833.25 ± 0.19	0.911 ± 0.016	0.064 ± 0.012	34.620 ± 0.013	55832.95 ± 0.26	-0.310 ± 0.026	0.209 ± 0.044	34.825 ± 0.045
2012E	55949.73 ± 0.79	1.343 ± 0.051	0.117 ± 0.026	34.682 ± 0.018	55948.57 ± 1.67	0.343 ± 0.162	0.200 ± 0.107	34.612 ± 0.111
2012cg	56082.40 ± 0.06	1.060 ± 0.006	0.173 ± 0.007	31.054 ± 0.006	56081.62 ± 0.06	-0.254 ± 0.021	0.543 ± 0.026	31.120 ± 0.035
2012dn	56132.44 ± 0.00	0.940 ± 0.028	0.458 ± 0.025	32.725 ± 0.023	56134.14 ± 0.57	-0.181 ± 0.050	0.841 ± 0.044	32.744 ± 0.076
2012ea	56158.17 ± 0.06	1.821 ± 0.000	0.389 ± 0.009	33.883 ± 0.009	56158.11 ± 0.07	1.396 ± 0.022	0.048 ± 0.029	33.496 ± 0.034
2013bs	56406.52 ± 0.22	1.507 ± 0.027	0.067 ± 0.016	35.516 ± 0.026	56406.28 ± 0.23	0.686 ± 0.062	0.031 ± 0.023	35.332 ± 0.071
2013dr	56486.38 ± 1.02	0.987 ± 0.089	0.153 ± 0.044	34.181 ± 0.174	56486.04 ± 1.44	-0.217 ± 0.080	0.332 ± 0.075	34.328 ± 0.160
2013dy	56501.48 ± 0.07	0.995 ± 0.006	0.123 ± 0.005	31.773 ± 0.008	56500.13 ± 0.06	-0.325 ± 0.016	0.420 ± 0.046	31.923 ± 0.040
2013ex	56529.48 ± 0.40	1.013 ± 0.030	0.044 ± 0.019	33.648 ± 0.033	56530.06 ± 0.60	-0.066 ± 0.051	0.142 ± 0.061	33.770 ± 0.067
2013fa	56536.19 ± 0.23	1.140 ± 0.023	0.297 ± 0.011	34.320 ± 0.018	56535.17 ± 0.46	-0.114 ± 0.037	0.607 ± 0.044	34.347 ± 0.053
2013fw	56601.68 ± 0.10	1.085 ± 0.014	0.031 ± 0.009	34.314 ± 0.014	56600.81 ± 0.09	-0.277 ± 0.027	0.189 ± 0.038	34.588 ± 0.043
2013gh	56529.10 ± 0.32	1.142 ± 0.032	0.366 ± 0.021	33.146 ± 0.028	56528.32 ± 0.08	0.112 ± 0.036	0.798 ± 0.034	32.808 ± 0.046
2013gq	56385.29 ± 0.18	1.233 ± 0.015	-0.003 ± 0.016	33.946 ± 0.029	56384.22 ± 0.17	0.008 ± 0.043	0.096 ± 0.040	34.119 ± 0.056
2013gy	56649.21 ± 0.12	1.125 ± 0.011	0.073 ± 0.012	34.024 ± 0.012	56648.36 ± 0.07	0.026 ± 0.032	0.280 ± 0.034	33.947 ± 0.044
2014J	56690.04 ± 0.13	0.952 ± 0.020	1.179 ± 0.014	28.415 ± 0.025	56689.20 ± 0.09	-0.219 ± 0.025	2.194 ± 0.048	27.865 ± 0.047
2014ai	56745.96 ± 0.23	1.490 ± 0.058	0.128 ± 0.025	35.097 ± 0.054	56744.75 ± 0.51	0.191 ± 0.124	0.277 ± 0.069	35.308 ± 0.115
2014ao	56766.17 ± 0.34	0.977 ± 0.032	0.820 ± 0.014	34.759 ± 0.033	56765.77 ± 0.61	-0.204 ± 0.088	1.441 ± 0.053	34.515 ± 0.076
2014bj	56796.73 ± 0.55	1.108 ± 0.038	0.044 ± 0.021	36.632 ± 0.024	56795.74 ± 0.65	-0.168 ± 0.071	0.169 ± 0.062	36.824 ± 0.078
2015N	57223.19 ± 0.15	1.087 ± 0.015	0.181 ± 0.012	33.877 ± 0.017	57222.89 ± 0.21	-0.134 ± 0.045	0.430 ± 0.142	33.865 ± 0.098
2016coj	57547.89 ± 0.23	1.131 ± 0.034	0.121 ± 0.018	32.306 ± 0.026	57547.83 ± 0.06	0.613 ± 0.033	0.024 ± 0.017	31.969 ± 0.042
2016fbk	57624.94 ± 0.41	0.993 ± 0.034	0.241 ± 0.016	36.180 ± 0.036	57625.09 ± 0.51	-0.046 ± 0.049	0.468 ± 0.046	36.156 ± 0.062
2016gcl	57649.84 ± 0.53	0.849 ± 0.024	0.025 ± 0.032	35.608 ± 0.056	57649.62 ± 0.38	-0.366 ± 0.029	0.126 ± 0.041	35.852 ± 0.050
2016gdt	57641.53 ± 1.08	1.822 ± 0.001	0.677 ± 0.064	35.832 ± 0.051	57640.11 ± 0.91	1.499 ± 0.077	0.147 ± 0.103	35.492 ± 0.076
2016hvl	57711.00 ± 0.12	1.123 ± 0.014	0.116 ± 0.012	33.420 ± 0.014	57709.48 ± 0.11	-0.281 ± 0.026	0.343 ± 0.115	33.634 ± 0.075
2017cfd	–	–	–	–	57844.39 ± 0.13	0.093 ± 0.048	0.504 ± 0.041	33.693 ± 0.058
2017drh	57890.60 ± 0.09	1.340 ± 0.011	1.601 ± 0.014	32.687 ± 0.013	57889.72 ± 0.10	0.112 ± 0.036	2.558 ± 0.045	32.169 ± 0.053
2017dws	57867.60 ± 1.20	0.882 ± 0.030	-0.051 ± 0.051	37.935 ± 0.038	57869.18 ± 1.29	-0.339 ± 0.091	0.075 ± 0.049	38.258 ± 0.135
2017erp	57935.15 ± 0.06	1.118 ± 0.006	0.099 ± 0.006	32.405 ± 0.006	57933.88 ± 0.06	-0.234 ± 0.021	0.444 ± 0.039	32.503 ± 0.039
2017fgc	57955.52 ± 0.38	0.840 ± 0.008	0.081 ± 0.016	32.775 ± 0.035	57955.78 ± 0.41	-0.324 ± 0.026	0.305 ± 0.033	32.866 ± 0.049
2017glx	–	–	–	–	58009.16 ± 0.16	-0.196 ± 0.025	0.174 ± 0.044	33.684 ± 0.044
2017hbi	–	–	–	–	58044.44 ± 0.14	-0.692 ± 0.017	0.186 ± 0.035	36.347 ± 0.041
2018aoz	58221.43 ± 0.14	1.283 ± 0.008	-0.079 ± 0.011	32.001 ± 0.014	58221.27 ± 0.19	0.187 ± 0.040	0.018 ± 0.012	32.107 ± 0.053
2018gv	58150.11 ± 0.08	1.006 ± 0.011	-0.046 ± 0.006	32.164 ± 0.013	58149.59 ± 0.11	-0.169 ± 0.024	0.035 ± 0.020	32.363 ± 0.038

Note. Only those SNe from our sample where the fitting process described in Section 5.2.1 or 5.2.2 succeeded appear here.

Table B3. Natural-system photometry of SN 2008ds.

SN	MJD	*B* (mag)	*V* (mag)	*R* (mag)	*I* (mag)	Clear (mag)	System
2008ds	54645.47	–	–	–	–	15.700 ± 0.033	KAIT4
2008ds	54646.47	–	–	–	–	15.574 ± 0.024	KAIT4
2008ds	54647.46	15.615 ± 0.012	15.629 ± 0.010	15.597 ± 0.011	15.742 ± 0.018	15.501 ± 0.010	KAIT4
2008ds	54650.47	15.501 ± 0.014	15.488 ± 0.010	15.476 ± 0.012	15.762 ± 0.015	–	KAIT4
2008ds	54653.13	15.482 ± 0.009	15.474 ± 0.005	15.418 ± 0.005	15.768 ± 0.008	–	Nickel1
2008ds	54653.44	15.489 ± 0.018	15.471 ± 0.010	15.439 ± 0.010	15.823 ± 0.016	–	KAIT4
2008ds	54655.13	15.565 ± 0.008	15.515 ± 0.006	15.456 ± 0.006	15.840 ± 0.009	–	Nickel1
2008ds	54655.48	15.559 ± 0.016	15.510 ± 0.012	15.471 ± 0.013	15.919 ± 0.022	–	KAIT4
2008ds	54658.13	15.695 ± 0.008	15.611 ± 0.006	15.548 ± 0.005	15.978 ± 0.008	–	Nickel1
2008ds	54662.16	15.975 ± 0.011	15.785 ± 0.005	–	–	–	Nickel1

Note. First 10 epochs of natural-system *BVRI* + unfiltered photometry of SN 2008ds. This table shows the form and content organization of a much larger table that covers each epoch of photometry for each SN in our data set. The full table is available in the online version of this article.

[1]*Department of Astronomy, University of California, Berkeley, CA 94720-3411, USA*

[2]*Department of Physics, University of California, Berkeley, CA 94720-7300, USA*

[3]*Miller Institute for Basic Research in Science, University of California, Berkeley, CA 94720, USA*

[4]*Harvard–Smithsonian Center for Astrophysics, 60 Garden Street, Cambridge, MA 02138, USA*

[5]*Gemini Observatory, 670 N. Aohoku Place, Hilo, HI 96720, USA*

[6]*Department of Physics and Astronomy, University of California, Los Angeles, CA 90095, USA*

[7]*Lawrence Berkeley National Laboratory, 1 Cyclotron Rd, Berkeley, CA 94720, USA*

[8]*Lick Observatory, PO Box 85, Mount Hamilton, CA 95140, USA*

[9]*Department of Astrophysical Sciences, Princeton University, 4 Ivy Lane, Princeton, NJ 08544, USA*

[10]*Department of Computer Science, Stanford University, 353 Serra Mall, Stanford, CA 94305, USA*

[11]*Netflix, Inc., 100 Winchester Cir, Los Gatos, CA 95032, USA*

[12]*NASA Jet Propulsion Laboratory, 4800 Oak Grove Dr, Pasadena, CA 91109, USA*

[13]*Department of Physics, Florida State University, Tallahassee, FL 32306, USA*

[14]*Department of Earth, Planetary, and Space Sciences, University of California, Los Angeles, CA 90025, USA*

[15]*Department of Mechanical and Aerospace Engineering, University of California, Los Angeles, CA 90025, USA*

[16]*Department of Physics and Astronomy, University of Wyoming, 1000 E. University, Dept 3905, Laramie, WY 82071, USA*

[17]*Department of Physics, Guangxi University, Nanning 530004, China*

[18]*Department of Physics and Astronomy, University of Oklahoma, 440 W. Brooks St., Norman, OK 73019, USA*

This paper has been typeset from a TEX/LATEX file prepared by the author.